Design and Fabrication of Monolithically-Integrated Laterally-Arrayed Multiple Band Gap Solar Cells using Composition-Graded Alloy Nanowires for Spectrum-Splitting Photovoltaic Systems

by

Derek Caselli

A Dissertation Presented in Partial Fulfillment
of the Requirements for the Degree
Doctor of Philosophy

Approved October 2014 by the
Graduate Supervisory Committee:

Cun-Zheng Ning, Chair
Meng Tao
Hongbin Yu
Dragica Vasileska

ARIZONA STATE UNIVERSITY

December 2014

ABSTRACT

This dissertation aims to demonstrate a new approach to fabricating solar cells for spectrum-splitting photovoltaic systems with the potential to reduce their cost and complexity of manufacturing, called Monolithically Integrated Laterally Arrayed Multiple Band gap (MILAMB) solar cells. Single crystal semiconductor alloy nanowire (NW) ensembles are grown with the alloy composition and band gap changing continuously across a broad range over the surface of a single substrate in a single, inexpensive growth step by the Dual-Gradient Method. The nanowire ensembles then serve as the absorbing materials in a set of solar cells for spectrum-splitting photovoltaic systems.

Preliminary design and simulation studies based on Anderson's model band line-ups were undertaken for CdPbS and InGaN alloys. Systems of six subcells obtained efficiencies in the 32-38% range for CdPbS and 34-40% for InGaN at 1-240 suns, though both materials systems require significant development before these results could be achieved experimentally. For an experimental demonstration, CdSSe was selected due to its availability. Proof-of-concept CdSSe nanowire ensemble solar cells with two subcells were fabricated simultaneously on one substrate. I-V characterization under 1 sun AM1.5G conditions yielded open-circuit voltages (V_{oc}) up to 307 and 173 mV and short-circuit current densities (J_{sc}) up to 0.091 and 0.974 mA/cm^2 for the CdS- and CdSe-rich cells, respectively. Similar thin film cells were also fabricated for comparison. The nanowire cells showed substantially higher V_{oc} than the film cells, which was attributed to higher material quality in the CdSSe absorber. I-V measurements were also conducted with optical filters to simulate a simple form of spectrum-splitting. The CdS-rich cells

showed uniformly higher V_{oc} and fill factor (FF) than the CdSe-rich cells, as expected due to their larger band gaps. This suggested higher power density was produced by the CdS-rich cells on the single-nanowire level, which is the principal benefit of spectrum-splitting. These results constitute a proof-of-concept experimental demonstration of the MILAMB approach to fabricating multiple cells for spectrum-splitting photovoltaics. Future systems based on this approach could help to reduce the cost and complexity of manufacturing spectrum-splitting photovoltaic systems and offer a low cost alternative to multi-junction tandems for achieving high efficiencies.

ACKNOWLEDGMENTS

I would like to acknowledge my advisor, Dr. Ning, for his guidance and support during my doctoral studies. I am also grateful to Patricia Nichols, Zhicheng Liu, Sunay Turkdogan, David Shelhammer, Leijun Yin, Kang Ding, and all the members of ASU Nanophotonics group for their advice, technical expertise, and assistance with various experiments. Their contributions were invaluable. I gratefully acknowledge the use of facilities within the Leroy Eyring Center for Solid State Science (CSSS) and Center for Solid State Electronics Research (CSSER) at ASU, as well as the research support staff for their help and dedication, especially Tim Karcher, David Wright, and Carrie Sinclair. Without their help, this dissertation would not have been possible. Financial support in the form of scholarships from the Science Foundation of Arizona and the ARCS Foundation, especially my sponsors Mr. and Mrs. Wilhoit, was enormously appreciated. Finally, I wish to thank all my friends and family for all their love and support, especially my wife Nicole Johannson.

TABLE OF CONTENTS

Page

CHAPTER Page

LIST OF TABLES

Table Page

LIST OF FIGURES

Figure Page

Figure Page

Figure Page

CHAPTER I

INTRODUCTION

I.A. Overview

Photovoltaic (PV) solar cells are a potentially attractive source of clean, renewable electricity, however their penetration into the general energy market has been hampered by the high cost of solar electricity. The cost of electricity produced by photovoltaic systems depends on both the cost and efficiency of the modules. In particular, efficiency is desirable both to decrease the cost per watt of the modules and to offset balance of systems costs, which tend to scale with system area. Multi-junction tandem cells, which currently represent the highest efficiency technology, consist of multiple solar cells with different band gaps fabricated in a many-layered vertical stack and connected in series by wide-band gap tunnel junctions. However, they require costly epitaxial growth techniques, and the requirement for lattice-matching among all layers of the device and substrate limits the selection of materials at the desired band gaps and makes it difficult to increase the efficiency by adding more junctions.

Spectrum-splitting photovoltaics aims to address these limitations by replacing vertically stacked multi-junction tandem cells with multiple cells of different band gaps placed side-by-side. A dispersive optical element (such as a prism) is used to split the incident sunlight into its spectral components and direct them towards different subcells of the appropriate band gaps. This greatly mitigates the lattice-matching problem, expanding the selection of possible materials and facilitating the addition of more junctions, potentially enabling higher efficiencies.

The first experimental spectrum-splitting PV system was demonstrated by Moon et al. in 1978 [1]. It consisted of separate Si and AlGaAs cells and achieved an efficiency of 28.5% under 165 times solar concentration, including optical losses [1]. More recently, researchers have demonstrated module efficiencies well over 30% [2]-[5] and are targeting efficiencies over 50% [6]-[8]. However, the traditional approach to spectrum-splitting PV involves manufacturing multiple cells on separate substrates using different materials and processes. As the number of cells increases, this quickly becomes complex and expensive. To the extent that the fabrication processes of the different cells could be merged, a significant advantage would be obtained.

Spatially composition-graded semiconductor alloy nanowires grown by a recently developed chemical vapor deposition (CVD) technique called the Dual Gradient Method [9]-[11] could provide just such an advantage. By engineering gradients in both the temperature and source vapor composition profiles across the surface of the substrate, local conditions are created which are conducive to the growth of different alloy compositions at different positions on the substrate surface [10],[11]. In this way, the alloy composition and semiconductor band gap can be continuously varied over a broad range across the surface of a single substrate in just a single, inexpensive growth step [10],[11]. The resulting nanowires could be used as the absorbing materials in a set of solar cells for a spectrum-splitting PV system [9]. This could potentially help to reduce the number of fabrication steps and unify the manufacturing processes of the various subcells, reducing the cost of the system accordingly.

Although in principle both nanowire ensembles and films may be grown by the Dual Gradient Method, nanowires are preferred for a mature system. Films permit simpler,

more facile fabrication and are therefore useful for the purpose of comparison with preliminary nanowire cells, however they are polycrystalline as grown by this technique and unsuitable for making high efficiency devices. Due to their small cross-sections and consequent tolerance for strain, nanowires can be grown with single-crystal quality even on lattice-mismatched or amorphous substrates. This is crucial for obtaining device quality materials across a broad range of compositions on a single substrate. It also permits the use of inexpensive substrates, which could be a key advantage for lowering costs. Another consequence of their small cross-sections is that nanowires can be synthesized with metastable compositions not possible in bulk materials. This further expands the selection of possible materials and band gaps. For these reasons, nanowires are more promising in the long term.

This dissertation focused on the design, simulation, fabrication, and characterization of solar cells for spectrum-splitting photovoltaic systems using spatially composition-graded semiconductor alloy nanowire materials. A set of six-subcells based on CdPbS alloys was designed and simulated. Efficiencies in the 32-38% range were obtained, depending on the level of solar concentration [12]. A similar study for InGaN found efficiencies varying greatly depending on the achievable carrier lifetimes and electron concentrations, but high efficiencies in the 34-40% range for 1-240 suns were found to be possible if sufficiently high quality materials can be synthesized [13]. However, for fabricating proof-of-concept devices, CdSSe was selected due to its availability. First, single solar cells based on pure CdSe nanowire ensembles and thin films were fabricated and characterized. Here, the performance of the film cells was found to be superior, with V_{oc} and J_{sc} up to 381 mV and 2.56 mA/cm^2 under 1 sun AM1.5G illumination,

respectively. This was attributed to longer carrier lifetimes in the films due to lower surface recombination and demonstrates the need for surface passivation in a practical system. Next, two subcells were fabricated simultaneously in a single process flow using spatially composition-graded CdSSe films and nanowire ensembles. In this case, the V_{oc} and FF of the nanowire cells exceeded those of the films, with the CdS- and CdSe-rich subcells achieving V_{oc} up to 307 and 173 mV and FF over 40% for both subcells. This was attributed to higher material quality in the nanowires than in the films and demonstrates the benefit of using nanowires for composition-graded cells in the long term. However, J_{sc} was somewhat lower for the nanowire cells due to spin-on glass covering some nanowires. I-V measurements were also taken using optical filters to simulate a simple form of spectrum-splitting and compare the subcells under similar levels of above-band gap photon flux. The CdS-rich cells achieved uniformly higher V_{oc} and FF than their CdSe-rich partner cells, as expected for the wider band gap subcell. This suggests that if all nanowires could be contacted for optimal current-matching between the cells, the CdS-rich cell should produce more power than the CdSe-rich cell, which is the chief benefit of spectrum-splitting that enables high efficiencies to be obtained. These results constitute a proof-of-concept demonstration of MILAMB solar cell fabrication with two subcells fabricated simultaneously on one substrate using spatially composition-graded alloy nanowires. In the future, this approach could potentially be used to produce a set of solar cells for spectrum-splitting photovoltaic systems at relatively low cost.

I.B. Theoretical Foundations

I.B.i. Basic Physics

The physical operation of a photovoltaic cell consists of two basic steps: photogeneration and charge separation. Incident photons with energy greater than the semiconductor band gap are absorbed, exciting electron-hole pairs in the material. In the presence of an electric field, the electrons and holes are accelerated in opposite directions, leading to a spatial charge separation. Depending on the load resistance, charge build-up and extraction may in general create both a voltage and a current (with open-circuit and short-circuit conditions being the limiting cases corresponding to zero current and voltage, respectively).

In practice, nearly all solar cells are semiconductor p-n junctions. Carriers generated within a diffusion length of the junction reach the space charge region and are separated by the electric field, creating a net current and an accumulation of electrons on the n-side of the junction and holes on the p-side. The photocurrent flows in the reverse-diode direction, whereas the charge build-up generates a voltage that forward-biases the junction. This implies that there are two opposing contributions to the current in a solar cell, one associated with photogeneration and charge separation (the photocurrent) and the other due to the forward-biased diode current. It is shown in the following section that the I-V characteristic of an ideal solar cell is identical to that of a diode, except that it is shifted by a constant photocurrent term.

I.B.ii. I-V Characteristic

The following is a basic derivation of the I-V characteristic of a p-n junction solar cell based on a problem statement from [14].

Consider the n^+p junction ($N_D >> N_A$) shown in Fig. I.B.1. Assume that the net electron-hole pair generation rate due to illumination is uniform throughout the structure and equal to G_L. Furthermore, let the device be weakly illuminated such that low-level injection conditions obtain, meaning that excess carrier concentrations (Δn and Δp, the carrier concentrations in excess of their equilibrium values) are much less than the equilibrium majority carrier concentrations, n_{n0} and $p_{p0,}$ but much greater than the equilibrium minority carrier concentrations, n_{p0} and p_{n0}. More concisely, n_{n0}, $p_{p0} >> \Delta n=\Delta p >> n_{p0}$, p_{n0}.

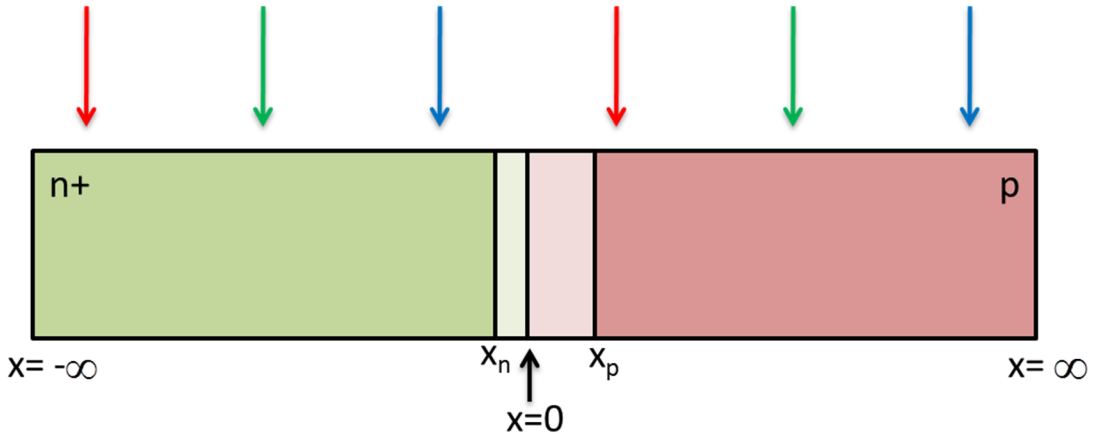

Figure I.B.1: An n^+p junction with infinite bulk regions on either side of the junction.

For a one-sided junction like that shown in Fig. I.B.1, the behavior of the device is controlled by the lightly doped side. Thus, it is sufficient to consider the p-type region. In the quasi-neutral bulk region, the magnitude of the electric field is negligible, therefore

charge transport is dominated by diffusion. The minority carrier diffusion equation on the p-side is:

$$\frac{\partial \Delta n_p}{\partial t} = D_n \frac{\partial^2 \Delta n_p}{\partial x^2} - \frac{\Delta n_p}{\tau_n} + G_L ,$$

where Δn_p is the excess electron concentration on the p-side of the junction. Under steady-state conditions, this reduces to:

$$0 = D_n \frac{\partial^2 \Delta n_p}{\partial x^2} - \frac{\Delta n_p}{\tau_n} + G_L .$$

This is an inhomogeneous differential equation, so the general solution is the sum of the homogeneous and particular solutions. The solution to the homogeneous equation consists of real exponentials:

$$\Delta n_{p,1} = A \exp\left(\frac{x'}{L_n}\right) + B \exp\left(-\frac{x'}{L_n}\right),$$

where $L_n = \sqrt{D_n \tau_n}$ and the coordinates are shifted for convenience using $x' = x - x_p$. An obvious particular solution is:

$$\Delta n_{p,2} = \tau_n G_L .$$

Thus, the general solution is:

$$\Delta n_p = A \exp\left(\frac{x'}{L_n}\right) + B \exp\left(-\frac{x'}{L_n}\right) + \tau_n G_L \qquad \text{(I.1)}$$

The next step is to apply boundary conditions. The first boundary condition is found by considering that far from the junction, the carrier concentration is uniform everywhere, so the second derivative with respect to x vanishes:

$$\lim_{x\to\infty}\frac{\partial^2\Delta n_p}{\partial x'^2}=0$$

$$\Delta n_p\left(x'=\infty\right)=\tau_n G_L \tag{I.2}$$

To find the second boundary condition, one employs the Law of the Junction at $x = x_p$, which states that the voltage across the depletion region is equal to the separation between the quasi-Fermi levels F_N and F_P, which are essentially constant in this region:

$$F_N - F_P = qV$$

Thus, the np product can be written:

$$np = n_i^{\,2}\exp\left(\frac{F_N-E_i}{k_BT}\right)\exp\left(\frac{E_i-F_P}{k_BT}\right)=n_i^{\,2}\exp\left(\frac{F_N-F_P}{k_BT}\right)=n_i^{\,2}\exp\left(\frac{qV}{k_BT}\right)$$

Low-level injection conditions obtain, per the stated assumption, so $p_p \approx p_{p0} \approx N_A$.

$$\Delta n_p\left(x'=0\right)=n_p-n_{p0}\approx\frac{n_i^{\,2}}{N_A}\left(\exp\left(\frac{qV}{k_BT}\right)-1\right) \tag{I.3}$$

Applying the condition in equation (I.2) to equation (I.1) gives:

$$\Delta n_p\left(x'=\infty\right)=\tau_n G_L = A\exp(\infty)+B(0)+\tau_n G_L$$

$$A\exp(\infty)=0$$

$$A=0$$

This gives:

$$\Delta n_p\left(x'\right)=B\exp\left(-\frac{x'}{L_n}\right)+\tau_n G_L \tag{I.4}$$

.

Applying equation (I.3) to equation (I.4) gives:

$$\Delta n_p\left(x'=0\right)=\frac{{n_i}^2}{N_A}\left(\exp\left(\frac{qV}{k_BT}\right)-1\right)=B\cdot\left(1\right)+\tau_n G_L$$

$$B=\frac{{n_i}^2}{N_A}\left(\exp\left(\frac{qV}{k_BT}\right)-1\right)-\tau_n G_L$$

$$\Delta n_p\left(x'\right)=\left[\frac{{n_i}^2}{N_A}\left(\exp\left(\frac{qV}{k_BT}\right)-1\right)-\tau_n G_L\right]\exp\left(-\frac{x'}{L_n}\right)+\tau_n G_L$$

At the edge of the depletion region $\left(x'=0\right)$, the magnitude of the electric field is negligible and the hole concentration is approximately equal to its equilibrium value everywhere in the p-type quasi-neutral region. Therefore, the current at this location is entirely due to electron diffusion and is equal to the current throughout the entire device under steady-state conditions (no charge build-up). Thus:

$$J=J_n\left(x'=0\right)\Big|_{diff}=qD_n\frac{d\Delta n_p\left(x'=0\right)}{dx'}$$

$$J=-\frac{qD_n{n_i}^2}{L_nN_A}\left(\exp\left(\frac{qV}{k_BT}\right)-1\right)+\frac{qD_nG_L\tau_n}{L_n} \qquad \text{(I.5)}$$

Grouping the terms and redefining the positive x-direction as the direction of forward-biased diode current flow gives:

$$J=J_S\left(\exp\left(\frac{qV}{k_BT}\right)-1\right)-J_L \qquad \text{(I.6)}$$

Here, J_S is the reverse saturation current density (also known as the dark current) and J_L is the light-generated current density. Notice that equation (I.6) is simply the ideal Shockley

diode equation shifted by the light-generated current density, which flows in the reverse-biased diode direction.

As for diodes, however, real devices typically deviate from equation (I.6) due to an empirical "ideality factor" which appears in the denominator of the exponential. Values of the ideality factor n vary in the range $1 \leq n \leq 2$, depending on whether recombination/generation in the quasi-neutral (n=1) or space charge region (n=2) dominates [15]. Also note that photogeneration in a real solar cell is non-uniform, decaying exponentially with depth as absorption attenuates the illumination. Thus, the current will differ somewhat from equation (I.5). Lastly, real solar cells often contain many non-idealities for which equation (I.6) does not account, including series and shunt resistances, surface recombination, and other effects.

A typical I-V curve for a silicon solar cell under air mass 1.5G illumination is shown in Fig. I.B.2 below. Per the convention, the positive current direction is taken to be opposite that for a diode, such that current produced by the cell is taken to flow in the positive direction.

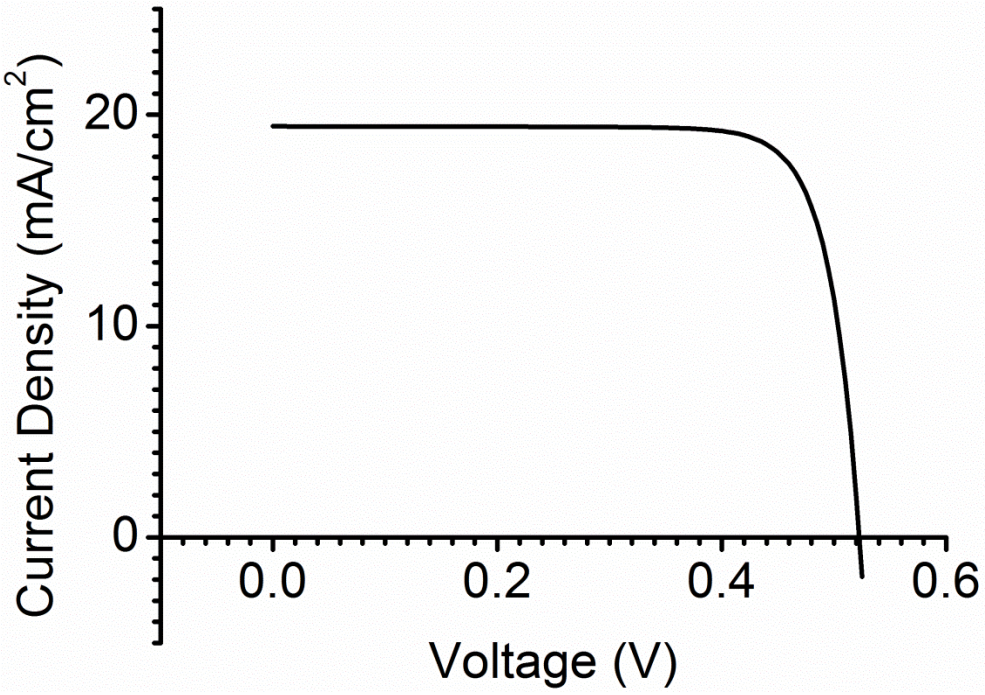

Figure I.B.2: I-V curve of a silicon solar cell simulated in Silvaco [16].

I.B.iii. Important Parameters: V_{oc}, I_{sc}, and FF

There are several important parameters of the I-V characteristic that are frequently used to characterize solar cells. These are short-circuit current (I_{sc}), open-circuit voltage (V_{oc}), and the fill factor (FF).

The short-circuit current is the output current from the cell when the output voltage equals zero. For commercial cells, the internal quantum efficiency – that is, the ratio of the number of electron-hole pairs extracted to the number of photons absorbed – is usually sufficiently high to approximate the short-circuit current as being equal to the light-generated current in equation (I.6) [17]. Assuming the internal quantum efficiency is constant with optical intensity, short-circuit current scales linearly with solar concentration [17].

The open-circuit voltage is the output voltage of the cell when the output current equals zero (or when the load resistance is infinite). An expression for V_{oc} is found by setting J=0 in equation (I.6):

$$V_{oc} = \frac{k_B T}{q} \ln\left(\frac{J_L}{J_S} + 1\right). \tag{I.7}$$

Note that V_{oc} increases logarithmically with the light-generated current density (and therefore with solar concentration) and decreases as the dark current increases. It does not increase linearly with temperature, as a cursory examination of equation (I.7) might suggest [17]. Rather, the dominant influence of temperature on V_{oc} actually enters equation (I.7) through the dark current due to its dependence on the square of the intrinsic carrier concentration; thus, V_{oc} actually decreases with increasing temperature [17].

Lastly, the fill factor is the ratio of the maximum output power of the cell to the product of V_{oc} and I_{sc}. Lower fill factors are often due to series or shunt resistance, though cells with larger band gaps tend to have larger fill factors. This is because semiconductors with larger band gaps have lower intrinsic carrier concentrations, leading to smaller dark currents and larger V_{oc} by equation (I.7). Larger V_{oc} causes the current-voltage characteristic to have a more rectangular shape, so the fill factor tends to increase with V_{oc}.

I.B.iv. Loss Mechanisms and the Shockley-Queisser Limit

There are many loss mechanisms that degrade the performance of solar cells, including series and shunt resistances, recombination, optical reflection, and temperature effects. Conceptually, two of the most important loss mechanisms are transmission and

thermalization loss. Transmission loss is the case wherein an incident photon has energy less than the band gap and so is not absorbed. Thus, the entirety of its energy is wasted (in practice, the situation is even worse, since these photons may be absorbed by packaging materials or through some intraband processes and raise the temperature of the cells). Thermalization loss occurs when an absorbed photon has energy in excess of the band gap. In this case, the photogenerated electron-hole pair quickly loses energy due to scattering events, causing each carrier type to decay to its respective band edge on picosecond time scales.

If the band gap is decreased, transmission loss decreases at the expense of increased thermalization loss, whereas increasing the band gap decreases thermalization loss at the expense of transmission loss. Thus, there is clearly an ideal value for the band gap of the absorbing material where the sum of thermalization and transmission loss is minimized. Shockley and Queisser find this value to be 1.1 eV for an idealized solar cell operating at the "ultimate efficiency", which is similar to the detailed balance limit for efficiency discussed below, albeit with idealized geometry and the cell temperature held at 0 K [18]. According to Henry [19], who alters Shockley and Queisser's analysis by using more realistic geometry and the measured solar spectrum rather than a blackbody approximation, the ideal band gap for a terrestrial, single junction solar cell is approximately 1.35 eV. However, the change in theoretical maximum efficiency with band gap depends upon the specific spectral conditions and assumptions employed, and the ideal band gap may vary somewhat as a result [20].

The most commonly cited theoretical efficiency limit for solar cells is known as the detailed balance limit and was first calculated by Shockley and Queisser [18] and later

revised by Henry [19]. The detailed balance limit is the maximum efficiency a p-n junction solar cell can achieve if the only loss mechanisms are transmission, thermalization, and radiative recombination (which is thermodynamically unavoidable) [18]. It further assumes that every above-band gap photon incident on the cell produces one electron-hole pair [18], thereby ignoring reflection, transmission (for $E_{photon} > E_g$), and more complicated effects such as two-photon absorption. Shockley and Queisser's analysis gives the detailed balance limit as 30% [18], whereas Henry finds it to be 31% when the measured air mass 1.5 solar spectrum is used in place of the blackbody approximation assumed by Shockley and Queisser [19]. Employing solar concentration or multiple absorbing materials with different band gaps increases this limit [19]. Using an infinite number of band gaps, the detailed balance efficiency of a solar cell is 68% without solar concentration and as much as 86% with maximal concentration (~45,900 times) [21].

I.C. Spectrum-Splitting Photovoltaics

Spectrum-splitting photovoltaics is an alternative to the multi-junction tandem approach that has been researched and discussed since the 1960s [22]. The concept, illustrated in Fig. I.C.1, is to use an optical element to split incident light into its spectral components and direct these to the most suitable cell among a set of solar cells with different band gaps. Placing the cells side-by-side, rather than in a vertical stack, mitigates the lattice-matching constraint and expands the selection of materials, allowing the design to be better optimized for efficiency. In addition, the lateral spectrum-splitting

design does not require tunnel junctions in order to achieve current-matching between cells, which simplifies their design and fabrication.

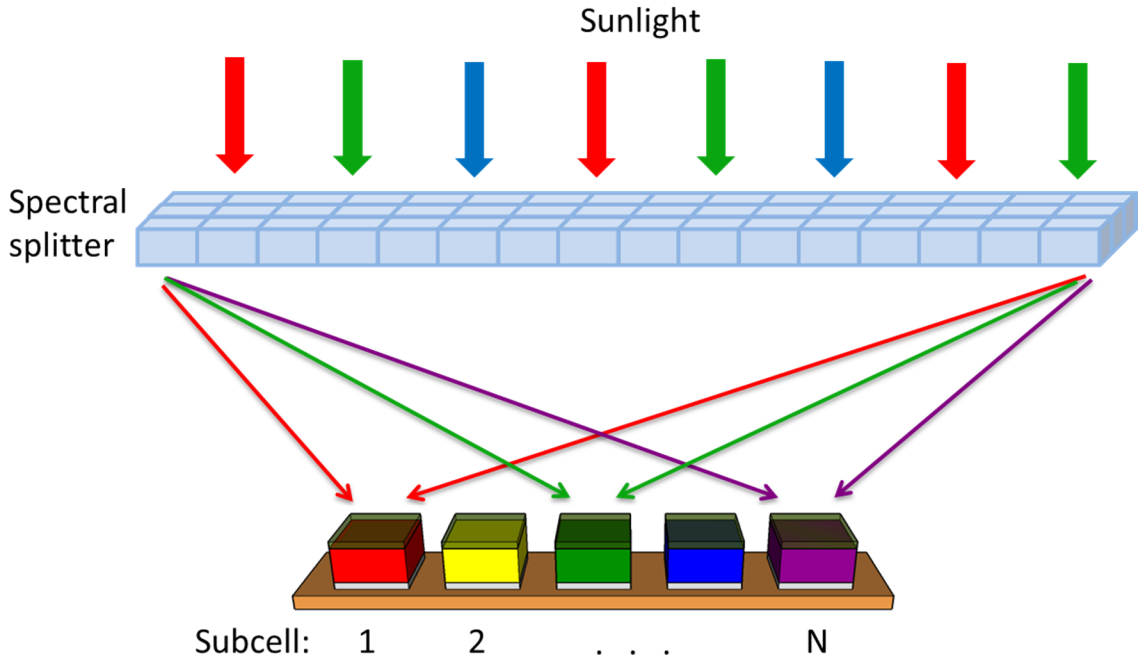

Figure I.C.1: Conceptual diagram of a spectrum-splitting photovoltaic system.

A number of different approaches to spectral splitting have been proposed, and an excellent review is provided by Imenes and Mills [22]. One of the more popular has been to use dichroic mirrors – many-layered stacks of dielectric materials which are highly reflective to wavelengths on one side of the cutoff wavelength and highly transmissive for wavelengths on the other [23]. Dichroic mirrors have high optical efficiency (often well above 90%) [23], which is crucial for solar applications and accounts for their popularity, but their reflective nature and the fact that each mirror can only split the incident spectrum into two components mean that the complexity of the system geometry increases rapidly with the number of subcells. Holographic dispersive concentrators

represent a potentially simpler option, enabling spectral splitting into many wavelength bands with a single optical element. These holograms are typically fabricated using dichromated gelatin [24],[25], which is suitably inexpensive for use in large areas [25]. Thus, transmission phase holograms may be viable for systems with low concentration ratios, whereas dichroic mirrors requiring stacks of perhaps hundreds [23] of dielectric layers are likely too expensive to be used in most applications outside of high concentration systems. Yet holographic spectral splitting with comparable optical efficiency to dichroic mirrors over a broad spectral range remains a goal of ongoing research.

In 1982, Bloss, Griesinger, and Reinhardt proposed using transmission phase holograms with high diffraction efficiency (the ratio of diffracted to incident power) and low absorption to simultaneously concentrate and spectrally split incident light [24]. They fabricated such holograms and measured the diffraction efficiencies as functions of wavelength and incident angle, showing that high optical efficiencies (>95%) could be obtained at specified wavelengths, though these decreased away from the peak wavelengths [24]. For a concentration ratio of 100, they estimated that a system utilizing a dispersive concentrator and three solar cells with band gaps of 0.9, 1.5 and 1.8 eV could achieve efficiencies as high as 42% [24]. No specific design was presented for such a system, however.

Ludman et al. describe a spectrum-splitting PV system utilizing GaAs and Si cells oriented perpendicular to a holographic dispersive concentrator [25]. In this case, the dispersive concentrator both divides the useful portion of the solar spectrum between the two cells and diverts infrared wavelengths that cannot be converted to electricity away

from them, preventing IR heating of the solar cells and relaxing the cooling requirements [25]. The cells are arranged perpendicular to the hologram because this configuration facilitates the rejection of these undesirable wavelengths [25]. Comparing with a more typical, non-dispersive concentrating PV module from Sandia National Labs which used Fresnel lenses to concentrate sunlight onto Si solar cells, the authors found that the proposed system could nearly double the power production and reduce the resulting cost of electricity by half [25].

More recently, publications [26]-[28] from a group led by Prof. Kostuk at the University of Arizona have described variations of a "holographic planar concentrator" utilizing transmission holograms and total internal reflection to provide low concentration ratios, spectral splitting, and possibly passive tracking. In this design, a transmitting or partially transmitting hologram is formed on top of or embedded within a layer of glass or plastic [26]-[28]. Incident light is diffracted at an angle which depends upon the wavelength, and light diffracted beyond the critical angle is guided by total internal reflection within the glass or plastic to a solar cell located at the edge [26]-[28]. This can provide low concentration (on the order of about 10 times) and spectral selectivity [26]-[28]. Spectral splitting can be achieved by stacking holographic planar concentrators [27],[28].

Refractive optics are yet another alternative. They utilize the dispersive properties of simple refractive elements such as prisms to achieve spectrum-splitting. One example is a dispersive lens design by Gu and Haney [29], wherein a thin layer of highly dispersive micro-prisms are integrated with a low dispersion lens. This allows spectrum-splitting over a broad wavelength range with relatively high optical efficiency (approximately

94% for the design presented), as well as providing solar concentration in an integrated optical element with flat-panel form factor [29].

The first experimental spectrum-splitting PV system was demonstrated by Moon and colleagues in 1978 [1]. It consisted of separate Si and AlGaAs cells and achieved an impressive efficiency of 28.5% under 165 times solar concentration, including optical losses [1]. Since that time, a number of other researchers have made significant strides in the field.

The most notable foray into the field was the recent Very High Efficiency Solar Cell (VHESC) project under DARPA [2],[4],[6],[7], where researchers proposed a design consisting of six subcells, including both discrete solar cells and tandem devices, with highly efficient (93%) spectrum-splitting optics based on dichroic mirrors and separate concentrators to provide a low solar concentration ratio of approximately 20 [7]. Based on the thermodynamic efficiency limit of a solar module with the planned band gaps, they estimated that the practical system efficiency, including optical losses, could reach 50% [7]. To date, submodule efficiencies as high as 36.7% have been verified by NREL under this program for a four-junction system consisting of two dual-junction tandem cells based on GaInP/GaAs and GaInAsP/GaInAs [4]. The optics for this system consisted of a concentrating lens and a dichroic beam splitter, which combined for a total optical efficiency of 89.1% [4]. Although the goal of 50% efficiency has not yet been realized, these preliminary results are promising for spectrum-splitting PV systems.

In 2011, Mitchell et al. demonstrated a four-subcell spectrum-splitting PV system using an elegant parallelepiped design based on dichroic mirrors to achieve 34% efficiency without solar concentration [3]. The structure was designed with dichroic

mirrors directly in front of each subcell, such that above band gap light was transmitted and below band gap light was reflected [3]. The subcells were positioned such that light reflected from one was incident on the next [3]. This configuration achieved an optical efficiency of approximately 94% [3]. The individual cells were a GaInP/GaAs tandem, a Si cell, and a GaSb cell [3]. Note that due to the geometry, the aperture area of the device is much smaller than the cell area, and therefore it must be used in conjunction with a separate solar concentrator [3].

While these approaches demonstrate the promise of spectrum-splitting PV for achieving high conversion efficiencies, the subcells must be fabricated individually on separate substrates. This requires a complex and potentially expensive manufacturing process. In this sense, there is room for improvement in cell technology to create more cost effective spectrum-splitting PV systems.

I.D. Spatially Composition-Graded Semiconductor Alloy Nanowires

Previous approaches to spectrum-splitting PV, as discussed above, typically combine solar cells produced through separate fabrication processes on different substrates with spectrum-splitting optics to achieve high efficiencies. However, using multiple different substrates and separate fabrication processes for each cell tends to drive up manufacturing costs. Ideally, the various fabrication processes should be integrated, such that many or all cells are fabricated simultaneously on a single substrate using inexpensive processes, while maintaining high material quality for optimum performance. Recent progress in the growth of semiconductor alloy nanowires may help to address this need.

In recent years, researchers in the ASU Nanophotonics group have demonstrated the capability to vary the composition of semiconductor alloy nanowires over a broad composition range across the surface of a substrate in a single, inexpensive CVD growth [10],[11],[30]. This is accomplished by means of the Dual-Gradient Method [11], which combines spatial reagent profiling with a temperature gradient across the surface of the substrate, as illustrated in Fig. I.D.1. Spatial reagent profiling to create a composition gradient in the source vapor was first used to successfully grow spatially composition-graded InGaN nanowires by Kuykendall et al. [31], but different material compositions were grown with the same nominal temperatures. In 2009, the ASU Nanophotonics group achieved continuous spatial composition grading of CdSSe nanowires using just a temperature gradient across the substrate surface (no source profiling) [10], demonstrating the validity of both approaches. To achieve alloy composition grading with maximum range and optimal material quality, morphology, flexibility, and control, it should be advantageous to combine both methods. In 2010, the resulting Dual-Gradient Method led to the demonstration of ZnCdSSe nanowires with compositions across virtually the entire composition range (from ZnS to CdSe), grown on a single substrate in one CVD growth run [11].

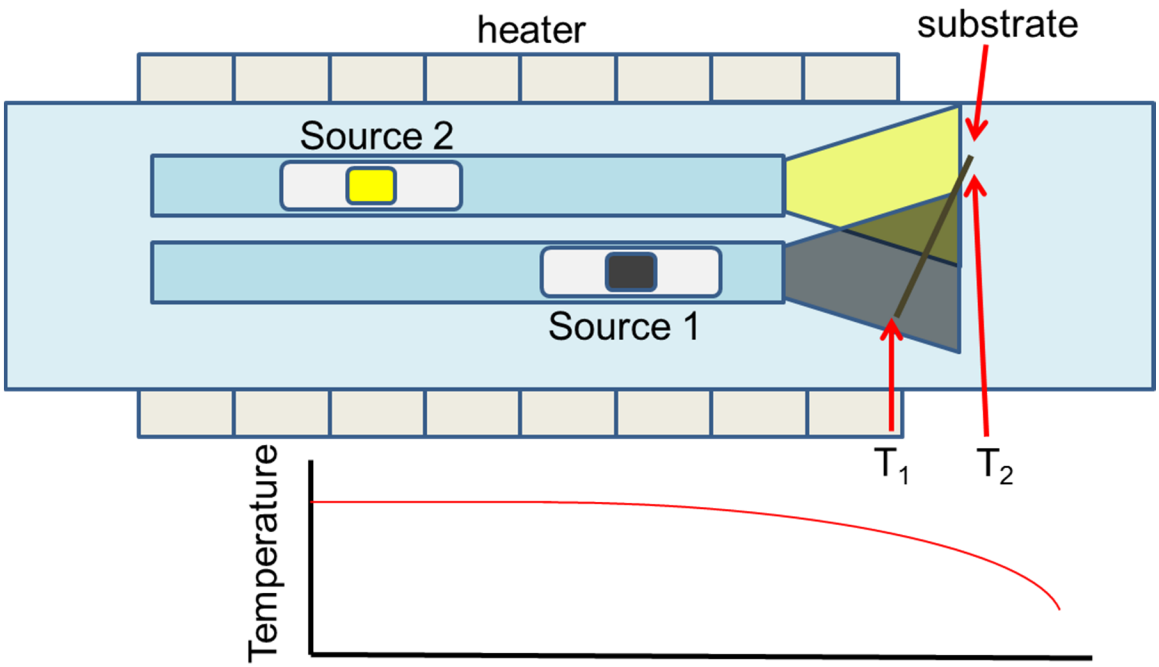

Figure I.D.1: Diagram of the experimental setup for Dual-Gradient growth [32].

Spatially composition-graded semiconductor alloy nanowires grown by the Dual-Gradient Method could potentially serve as cost-effective absorbing materials in solar cells for spectrum-splitting PV systems. In the next section, theoretical designs and simulations are presented for solar cells based on composition-graded CdPbS and InGaN alloys.

CHAPTER II

THEORETICAL MILAMB CELL DESIGN AND SIMULATION

Theoretical MILAMB cells were designed and simulated in order to assess the potential of some possible implementations of this concept. This study focused on two materials systems: CdPbS and InGaN. CdPbS or InGaN nanowires grown by the Dual-Gradient Method have the potential to span the entire range of band gaps of interest for photovoltaics and could be produced in a single CVD growth on a single substrate. The synthesis of spatially composition-graded CdPbS nanowires across the full alloy composition range has not been demonstrated to date, but may be possible by exploiting the unique advantages of nanowires over the bulk and thin film materials used by previous researchers. More specifically, the small cross sections and non-equilibrium vapor-liquid-solid growth of nanowires permit metastable alloys to be grown with compositions forbidden in bulk or film materials. So far, $Cd_xPb_{1-x}S$ nanowires with x up to 0.14 have been demonstrated [33], while InGaN nanowires with compositions across the full alloy range have been grown [31].

Simulations performed using Silvaco ATLAS [16] software found efficiencies in the 32-38% range for a system of six cells based on CdPbS alloys, depending on the level of solar concentration [12]. A similar study for InGaN found that the achievable efficiencies depended strongly on the carrier lifetime and electron concentration in the InGaN absorber, with efficiencies in the 20-27% range for typical 1 ns lifetimes and rising to 34-40% for more optimistic lifetimes of 10 ns. The designs for both materials systems showed the potential for achieving even higher efficiencies with additional optimization. They are discussed in detail in section II.A for CdPbS and II.B for InGaN.

II.A. CdPbS

One possible materials system for implementing the MILAMB solar cell concept is CdPbS. As previously discussed, $Cd_xPb_{1-x}S$ materials with compositions across the full alloy range $0 < x < 1$ have not yet been achieved, but may be possible in nanowire morphology [33]. If this goal can be achieved, CdPbS alloys would provide band gaps from 0.4 to 2.4 eV [34]-[37], spanning the entire range of interest for photovoltaics. This could make it an interesting option for MILAMB solar cells in high efficiency spectrum-splitting PV systems, where the Dual-Gradient growth of CdPbS absorbing materials could enable reductions in the cost and complexity of fabrication.

In this section, a set of six p-i-n heterojunction solar cells with CdPbS absorbers was designed and simulated, as discussed in a recent publication [12]. The efficiency of this system varied from 32% at 1 sun to 38% at 240 suns. This suggests these cells have the potential to achieve high efficiencies in the range of existing multi-junction tandems. Nonetheless, the performance was somewhat lower than would be anticipated for a system of six subcells. This was due to the effects of band offsets arising from limited material options and necessary design compromises between structural simplicity and performance. Simulations were also conducted with reduced carrier mobilities to probe the effects of possible surface scattering in the nanowires. Reducing the carrier mobilities to 50% and 25% of their full (interpolated) values predictably decreased the efficiency, roughly by 1-2% (absolute) at 1 sun but by increasingly greater margins at higher concentration levels. This was attributed to increased resistive losses at higher concentration levels. The results suggest that if composition-graded CdPbS nanowires

can be synthesized across the full alloy range, they could be an attractive option for fabricating spectrum-splitting PV cells at low cost. However, due to the inherent unreliability of Anderson's model for predicting band alignments, experimental studies of the materials will be required to verify the properties of the heterojunctions employed in this design.

II.A.i. Design

The first step in designing a set of CdPbS solar cells for a spectrum-splitting PV system was to select the band gaps of the subcells. CdPbS can in principle achieve band gaps from 0.4 (PbS) to 2.4 eV (CdS) [34]-[37], though the range of alloy compositions achieved so far is limited [33]. For the present design, six subcells were selected with a minimum band gap of 0.7 eV. The band gaps were selected for current-matching in series connection, where the current of the string cannot exceed the smallest current produced by an individual subcell. Assuming the quantum efficiencies of all subcells are approximately equal, this requires selecting band gaps such that each subcell receives an equal flux of above-band gap photons. The resulting band gap selections are listed in Table II.A.1. Note that the corresponding compositions are calculated under the assumption that the band gap varies linearly with composition fraction (a bowing parameter of zero), and are therefore only tentative values.

Table II.A.1: Band gaps optimized for current matching and the corresponding electron affinities and alloy compositions, assuming a linear relationship between band gap and composition fraction

Subcell	Composition	Band gap Energy (eV)	Electron Affinity (eV)
1	$Cd_{0.89}Pb_{0.11}S$	2.17	4.36
2	$Cd_{0.76}Pb_{0.24}S$	1.74	4.11
3	$Cd_{0.52}Pb_{0.48}S$	1.43	3.93
4	$Cd_{0.39}Pb_{0.61}S$	1.17	3.77
5	$Cd_{0.28}Pb_{0.72}S$	0.95	3.64
6	$Cd_{0.16}Pb_{0.84}S$	0.70	3.50

With the band gaps of the absorbing materials determined, the next step in the design is to provide for charge separation and extraction. For this purpose, a p-i-n heterojunction cell structure was selected. Doping CdPbS both n- and p-type would likely prove problematic for at least some alloy compositions (CdS is not readily p-dopable due to native defects and compensation effects [38]), making a homojunction structure difficult to realize. Furthermore, even with surface passivation, carrier lifetimes in the nanowires could prove to be lower than desired. Typical p-n junction solar cells allow carriers to diffuse to the junction before they are separated, but for devices with shorter minority carrier lifetimes it is often beneficial to use drift to speed carrier extraction. Thus, a p-i-n structure with intrinsic CdPbS and highly doped semiconductor n- and p-layers is the best choice.

Several factors are important to the choice of n- and p-layer materials. Firstly, the top layer must be transparent for light to reach the absorbing materials, so it must have a significantly wider band gap than the widest band gap CdPbS nanowires. At the same time, it must be sufficiently conducting to minimize series resistance during lateral

conduction to the final metal contacts. Secondly, the band offsets of both layers with the CdPbS band edge from which carriers are to be extracted (e.g. the conduction band for an n-layer) must be minimal. This ensures that carriers of the designated type can readily flow into the doped layer. Thirdly, they should be capable of achieving high doping concentrations (~10^{18} cm^{-3} or greater) in order to facilitate the formation of ohmic contacts with the final metal electrodes. Finally, wherever possible, the same materials should be used for different subcells to simplify the fabrication process and minimize manufacturing costs.

With these constraints in mind, the contacts were selected as shown in Fig. II.A.1, which displays the energy band alignments for all subcells. The top n-contact material was chosen to be ZnS because it has a suitably large band gap at 3.66 eV, and its electron affinity of 3.9 eV [37] is a workable compromise between those of the CdPbS alloys in the first and sixth subcells, allowing it to be used for all subcells. However, while it is capable of moderately high doping levels on the order of 10^{19} cm^{-3}, this requires advanced techniques and is difficult to achieve [38]. It is more typically a highly resistive material unsuited for lateral conduction of current to the final metal contacts. Indium tin oxide (ITO) is a transparent conductor with an electron affinity of approximately 4.7 eV, far too large to serve as the primary top contact material in this application, but its conductivity is far greater than that achievable with ZnS [39],[40]. Depositing ITO atop the n-ZnS contact can dramatically reduce the series resistance and improve device performance.

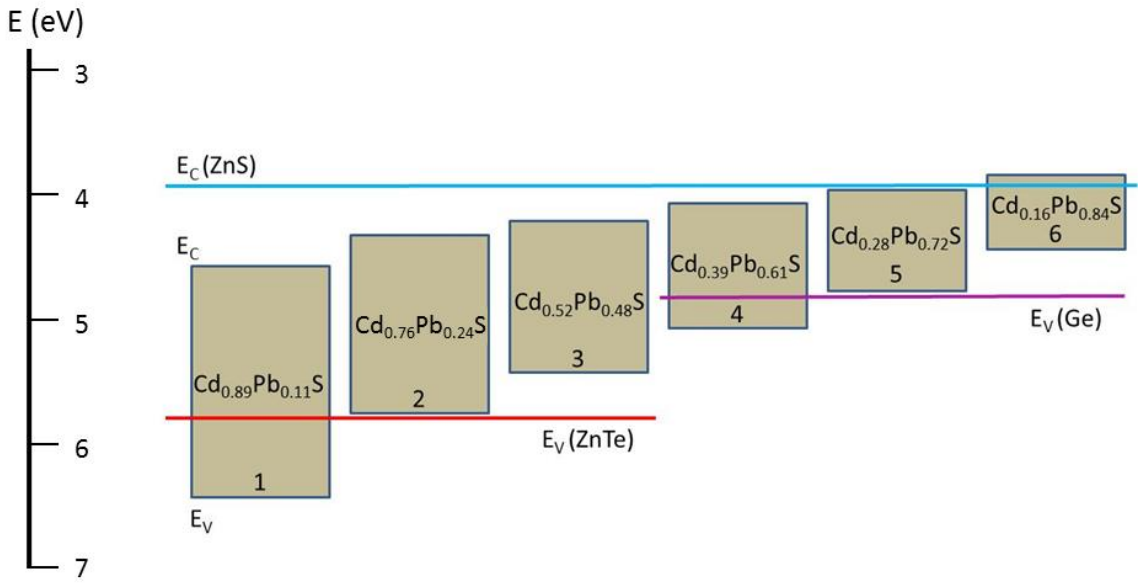

Figure II.A.1: Tentative band alignments for CdPbS solar cells.

The p-contacts are more challenging because the valence band edge of CdPbS varies over a wider range with composition fraction according to Anderson's model than does the conduction band (see Table II.A.1). This means that it is not possible to use a single p-contact material across all subcells. ZnTe has a band gap and electron affinity of approximately 2.26 eV and 3.5 eV respectively [41],[42], giving it an acceptable valence band alignment with the three larger band gap subcells (see Fig. II.A.1). Unlike virtually any other II-VI material, it can also be readily p-doped up to high acceptor concentrations [38], making it uniquely suited for this application. Note, however, that the valence band discontinuity of ZnTe with CdPbS in the largest band gap subcell (subcell 1 in Fig. II.A.1) is significant. Although this is not fatal, it does have a significant detrimental effect which will be examined in more detail later.

For the three smallest band gap subcells, the valence band edge of ZnTe is far too low. Ge, with a band gap and electron affinity of 0.66 eV and 4.0 eV respectively [43] represents the best alternative. However, even Ge presents a barrier to hole extraction for

the two smallest band gap subcells (subcells 5 and 6 in Fig. II.A.1). This is undesirable, but it represents an acceptable compromise under the constraints discussed above.

II.A.ii. Silvaco ATLAS Simulations

Each subcell in this design was simulated separately using Silvaco ATLAS software [16], and then the overall performance with subcells connected in series was calculated.

The illumination source was the ASTM G173 air mass 1.5 direct (AM1.5D) spectrum, as provided by the National Renewable Energy Laboratory (NREL) [43]. The AM1.5D spectrum includes only light incident directly from the solar disk and excludes light scattered from other portions of the sky; this scattered light is called diffuse sunlight and is included in the air mass 1.5 global (AM1.5G) spectrum. The AM1.5D spectrum is the standard spectrum used to compare terrestrial concentrating PV systems because solar concentrators have limited acceptance angles, meaning that high concentration systems require two-axis solar tracking and reject diffuse sunlight.

Since this study focused on the cells rather than the dispersive concentrator, the optics were assumed to be 100% efficient. Furthermore, no reflection was considered at the top interface. Thus, the simulations yielded the efficiency with which light that penetrates into the subcells is converted to electricity, but this must be multiplied by the optical efficiency to find the overall system efficiency.

The areas of all subcells were assumed to be equal, such that the concentration ratios for all subcells within their assigned spectral bands were identical. Simulations were conducted for concentration ratios of one, 25, 100, and 240, where the concentration ratio is defined as the area of the solar collector divided by the total solar cell area. Since

incident sunlight was spectrally split between six subcells, this definition implies that the spectral band assigned to a given subcell was effectively concentrated by a factor of six for a nominal concentration ratio of one.

Furthermore, for practical reasons, the compositions of the absorbing layers were treated as being constant within each subcell. This avoided the issue of matching the exact optical dispersion pattern with the composition gradient of the alloy nanowires. In practice, they would need to be matched through optimized optical design and controlled composition-graded nanowire growth.

In practice, simulating the nanowire geometry of the absorbing layer is difficult. Nanowires are known to experience significant absorption enhancement due to their small, often sub-wavelength dimensions and light trapping effects, in some cases exceeding the absorption of comparable thin films [45],[46]. The optical absorption of a nanowire array compared to a thin film of the same composition depends upon the nanowire geometry, array density, and the incident angle of incoming radiation [45],[46]. Optimization of the geometric characteristics of the nanowire array was not the goal of these simulations. Therefore, since an appropriately optimized array should at least match the optical absorption of a comparable film, the CdPbS nanowire ensembles were treated as thin films for simplicity.

Another possible way in which the nanowire geometry may influence the performance of the cells is by decreasing the carrier mobilities through enhanced surface scattering. The mobility of minority carriers is directly proportional to the diffusion coefficient, which affects the diffusion length. Decreasing the diffusion length could result in a greater number of carriers recombining before reaching the space charge region, reducing

the efficiency. The sensitivity of the cells to this effect was studied by decreasing the mobilities to 50% and 25% of their full (interpolated) values. The effect was found to be tolerably small, as discussed in Section II.A.iii. (Results and Discussion) and reported in Table II.A.2.

Shockley-Read-Hall recombination was assumed to dominate, and fixed carrier lifetimes of 10 ns were chosen based on a measurement performed on CdSSe nanowires.

Finally, the semiconductor contacts were assumed to be doped up to 10^{19} cm^{-3}, with metal electrodes forming ideal ohmic contacts to each. Both the top and bottom metal electrodes completely covered the respective surfaces, so no series resistance due to lateral conduction through the top semiconductor contact was considered (equivalently, the ITO layer was assumed to be perfectly conducting).

II.A.iii. Results and Discussion

The open-circuit voltages, short-circuit currents, fill factors, and conversion efficiencies of the MILAMB solar cell under various levels of solar concentration and reduced carrier mobilities are shown in Table II.A.2. These simulations showed the MILAMB solar cell reaching efficiencies in the high 30% range at low concentration levels, albeit with the assumptions noted above, near existing tandem cells on the market today. At one sun illumination conditions, the effect of reducing the carrier mobilities was relatively small, but it became more significant under higher levels of solar concentration. For the simulations where carrier mobilities were set to 50% and 25% of their interpolated values, the efficiencies began to peak at lower levels of solar

concentration. This is due to increased resistive losses, which scale with the square of the current (I^2R), which is linearly proportional to intensity [17].

Table II.A.2: MILAMB solar cell efficiencies, fill factors, open-circuit voltages, and short-circuit current densities at various levels of solar concentration and reduced carrier mobilities

Mobilities	Concentration	Efficiency	Fill Factor	V_{oc} (V)	J_{sc} (mA/cm^2)
100%	1	31.8%	75.8%	4.760	7.930
100%	25	36.8%	76.0%	5.495	198.3
100%	100	38.7%	75.0%	5.852	793.1
100%	240	38.0%	71.1%	6.085	1899
50%	1	30.8%	73.9%	4.776	7.864
50%	25	35.8%	74.1%	5.516	196.7
50%	100	36.7%	71.4%	5.877	786.7
50%	240	33.9%	63.9%	6.110	1876
25%	1	29.6%	71.9%	4.788	7.738
25%	25	34.1%	71.4%	5.538	193.9
25%	100	33.8%	66.6%	5.899	774.6
25%	240	29.3%	57.4%	6.131	1799

For a more detailed examination of the MILAMB cell's performance, Fig. II.A.2 shows the I-V characteristics at one sun illumination for the case where the carrier mobilities are not reduced. One of the most readily apparent features of these plots is the unusual shape of the curve for the largest band gap subcell, designated subcell 1 in Fig. II.A.2, whereby the current approaches zero for large voltages rather than displaying the typical exponential diode behavior. This is a phenomenon known as "roll-over" and is caused by the large valence band offset between ZnTe and CdPbS, as seen in Fig. II.A.1. The valence band edge of ZnTe is significantly higher than that of the CdPbS, meaning that large forward biases tend to drop mostly at the CdPbS/ZnTe interface and do not significantly affect the current [47]. This decreases the fill factor and causes the flattening of the I-V curves observed in Fig. II.A.2. This harms the performance of the first subcell

and decreases the power conversion efficiency of the MILAMB solar cell. Replacing ZnTe with another p-type semiconductor with a smaller valence band offset with CdPbS would improve device performance, but the selection of materials for this application is extremely limited. Furthermore, improving the valence band alignment between CdPbS and the p-layer for subcell 1 would have a detrimental effect on the alignment with subcell 3 unless separate contact materials were chosen for each of these subcells. Further analysis would be required to determine if the resulting increase in the complexity of the manufacturing process and the associated rise in cost would justify the change.

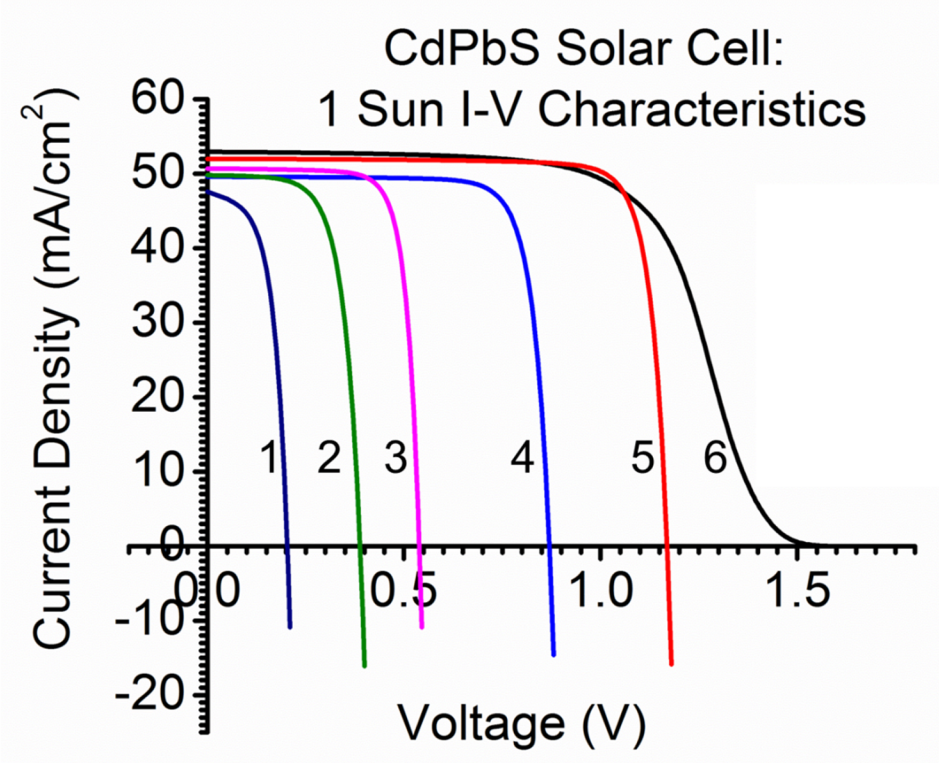

Figure II.A.2: I-V characteristics of the MILAMB solar cell with 100% carrier mobilities under various levels of solar concentration.

Furthermore, note that the sixth subcell (with the smallest band gap) is current-limiting. This is primarily due to the poor valence band alignment with the p-contact

leading to incomplete carrier collection. Fig. II.A.1 shows that the valence band edge of Ge is significantly lower than that of CdPbS in the sixth subcell, creating a barrier for hole extraction. As with the first subcell, this is the result of an inevitable compromise between efficiency and structural simplicity during selection of the contact material, in addition to the limited number of material options.

Despite some necessary design compromises, the efficiencies listed in Table II.A.2 attest to the MILAMB solar cell's potential to achieve relatively high conversion efficiencies. Moreover, the ability to fabricate many of its constituent subcells simultaneously (in two groups) in a more integrated manufacturing process could potentially permit lower costs than other spectrum-splitting PV modules.

II.A.iv. Conclusion

A set of six p-i-n solar cells with CdPbS absorbers for a spectrum-splitting PV system was designed and simulated. Efficiencies in the range of 32-38% were achieved under AM1.5D illumination with concentration ratios ranging from 1-240 suns. The I-V curves of some subcells showed detrimental effects (such as roll-over) of relatively large band offsets due to design compromises made to maintain structural simplicity. Nonetheless, relatively high efficiencies were obtained. Combined with the potential to grow the nanowire absorbing materials on a single, inexpensive substrate and integrate the fabrication processes of many of the subcells, this could make MILAMB solar cells based on CdPbS nanowires an attractive option for future spectrum-splitting PV systems.

In the discussion in the following section, a design for the InGaN materials system is considered.

II.B. InGaN

In addition to CdPbS, MILAMB solar cells could also be realized using InGaN nanowires. InGaN alloys are of great interest for high efficiency PV due to the wide range of band gaps they can achieve, from 0.7 to 3.4 eV [48], which includes all band gaps of interest for PV applications. InGaN has received considerable attention from the PV community for this reason, but it is not suitable for traditional high efficiency tandem cells. This is because its lattice constant varies widely with composition, preventing lattice-matching between layers, and InGaN has a miscibility gap which prohibits many useful band gaps from being utilized in materials with traditional film morphology. However, InGaN nanowires grown by Dual-Gradient CVD for spectrum-splitting PV could potentially overcome these barriers. Researchers using a related method have demonstrated the ability to grow $In_xGa_{1-x}N$ nanowire ensembles with compositions graded across the entire range $0 < x < 1$ along the surface of a single substrate, although the absorption edge remained above 1.0 eV even for pure InN [31]. The nanowires were able to bridge the miscibility gap due to their small cross sections and the non-equilibrium growth, which permit metastable alloys to be grown with compositions forbidden in bulk material. These could be used as the absorbing materials in a set of solar cells for a spectrum-splitting PV system, where they could enable the fabrication processes of the different subcells to be integrated, greatly simplifying the manufacturing and offering a potential cost advantage.

InGaN solar cells with three and six subcells were designed and simulated [13] using Silvaco ATLAS software [16]. Simulations assuming a minority carrier lifetime of 1 ns

(realistic for present InGaN materials [43],[49],[50]) showed relatively low efficiencies relative to the number of subcells, around 20% under 1 sun AM1.5D conditions and approximately 25% at 240 suns for six subcells. However, when the carrier lifetime was allowed to increase to 10 ns, the efficiency rose dramatically, with values in the 34-40% range, depending on the level of solar concentration. This suggests the material quality and carrier lifetimes in the InGaN nanowires would be crucial for obtaining high efficiencies in a practical system. It was also found that the efficiencies for three subcells were very similar to those for six subcells. This was due to variations in the quantum efficiencies of the subcells which exacerbated current mismatch in the six-cell design. This could be resolved by redesigning the band gaps of the cells to account for the variation of quantum efficiency with InGaN composition, as would likely be necessary in any practical system anyway to deal with various other non-idealities that might occur.

II.B.i. Design

The basic design criteria for InGaN MILAMB cells were similar to those described in Section II.A.i. in connection with the CdPbS MILAMB cell design. The first task in designing a set of InGaN cells for a spectrum-splitting PV system was to select the desired band gaps for the different subcells. A simple series-connection scheme requires current-matching between the cells. Assuming similar quantum efficiencies for all cells in the system, this was achieved by assigning spectral bins to the different cells such that each received the same photon flux, as for the CdPbS design. The longest wavelength in each bin determined the band gap of the corresponding cell. Given a six-subcell system with a minimum band gap of 0.7 eV (pure InN), this specified the band gaps of each of

the subcells as shown in Table II.B.1. A simpler three-subcell design was obtained using only the even-numbered subcells. InN and GaN have band gaps of approximately 0.7 eV and 3.4 eV [48], and their electron affinities are most commonly reported as 5.5 eV and 3.5 eV, respectively [51]-[53]. The bowing parameters from [48] for the band gap and electron affinity of InGaN as a function of composition were used to calculate the electron affinities and alloy compositions from the band gaps.

Table II.B.1: InGaN band gaps, electron affinities, and alloy compositions for a set of six current-matched cells, calculated using bowing parameters from [48].

Subcell	Band Gap (eV)	Electron Affinity (eV)	$In_xGa_{1-x}N$ Composition (x)
1	2.17	4.00	0.3372
2	1.74	4.27	0.4826
3	1.43	4.51	0.6028
4	1.17	4.78	0.7189
5	0.95	5.06	0.8341
6	0.70	5.50	1.0000

Next, the basic cell structure was determined. One of the challenges of InGaN materials, particularly for the In-rich compositions necessary for a high-efficiency PV system, is the difficulty of p-type doping. GaN can be p-doped using Mg up to an effective acceptor concentration on the order of 10^{18} cm^{-3}, but the difficulty increases rapidly with In content, and In-rich InGaN is typically highly n-type even without intentional doping [48]. Thus, creating a p-n homojunction device is not yet a practical possibility. Many wide-band gap InGaN solar cells in literature use a p-type GaN layer to form a p-n or p-i-n junction with InGaN, but the valence band offset between GaN and In-rich InGaN is too large for efficient charge separation [48].

However, preliminary predictions based on a simple electron affinity band alignment model suggest that the valence band offset of GaP with In-rich InGaN is relatively small

across a fairly broad range of compositions, as shown schematically in Fig. II.B.1. GaP can be doped p-type up to high acceptor concentrations (above 10^{19} cm^{-3}) [54] and has an electron affinity and indirect band gap of 3.8 eV and 2.26 eV [43], respectively, which would allow it to be used as a p-type layer and heterojunction partner for separating charge carriers generated in n-type InGaN (analogous to the role of CdS in thin film solar cells). The band gap of GaP is smaller than desired for this application and led to some detrimental absorption in this layer, but overall it was found to be an acceptable design compromise.

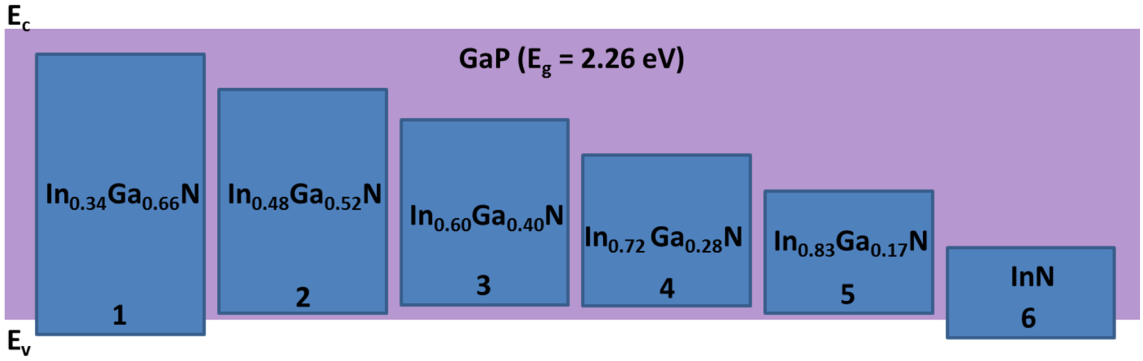

Figure II.B.1: Band alignment of GaP with the InGaN cells as shown in [13] and described in Table II.B.1. A three subcell design is obtained using only the even-numbered cells.

Thus, a set of solar cells was designed which consisted of p-n heterojunctions between n-type InGaN nanowires of widely varying compositions and p-type GaP.

II.B.ii. Simulation Results and Discussion

Device simulations of this structure under illumination by the ASTM G173 standard AM1.5D spectrum were conducted using Silvaco ATLAS software [16]. Similar simplifying assumptions were made as in previous work [12], including no optical losses in the dispersive concentrator, ideal ohmic electrodes, no resistive losses in the contacts,

equal area subcells, fixed carrier lifetimes, uniform material composition within any given subcell, and treatment of the dense nanowire array as a continuous film.

An effective donor concentration in the InGaN of 10^{18} cm^{-3} was assumed, while the acceptor concentration in the p-GaP layer was taken to be 10^{19} cm^{-3}. The InGaN nanowires were modeled as a 1.7 μm thick film, and the GaP was taken to be 100 nm thick.

Simulations were conducted for solar concentration ratios from one to 240 suns with carrier lifetimes of 1 and 10 ns. The results are shown for the six- and three-cell designs in Table II.B.2 and II.B.3, respectively. The three-cell design achieved performance roughly on par with the six-cell design, with both achieving roughly 20% efficiency at 1 sun for 1 ns lifetimes and 33-34% for 10ns lifetimes. This was due to variations in the quantum efficiencies of the subcells which created greater current mismatch losses in the six-subcell design than in the three-subcell design, compensating the lower thermalization losses from having more cells. This is demonstrated in Tables II.B.4 and II.B.5, which compare the short-circuit currents of the various subcells for the six- and three-subcell cases, respectively [13]. In the case of six subcells (Table II.B.4), the difference between the highest and lowest J_{sc} was 5.9 mA/cm^2, whereas the largest mismatch was only 1.2 mA/cm^2 for three subcells (Table II.B.5).

Table II.B.2: Performance of the six-cell InGaN design as a function of solar concentration ratio for carrier lifetimes of 1 ns and 10 ns

Solar Concentration Ratio	Efficiency (τ = 1 ns)	Efficiency (τ = 10 ns)
1	19.9%	33.8%
25	23.2%	38.0%
100	24.5%	39.5%
240	25.2%	40.4%

Table II.B.3: Performance of the three-cell InGaN design as a function of solar concentration ratio for carrier lifetimes of 1 ns and 10 ns

Solar Concentration Ratio	Efficiency (τ = 1 ns)	Efficiency (τ = 10 ns)
1	20.6%	32.9%
25	24.8%	37.3%
100	26.4%	39.1%
240	27.2%	40.2%

Table II.B.4: Short-circuit current densities of the six-cell InGaN MILAMB subcells at 1 sun operation for 10 ns carrier lifetimes

Subcell	J_{sc} (mA/cm^2)
1	41.5
2	39.3
3	38.2
4	36.7
5	35.8
6	35.6

Table II.B.5 Short-circuit current densities of the three-cell InGaN MILAMB subcells at 1 sun operation for 10 ns carrier lifetimes

Subcell	J_{sc} (mA/cm^2)
1	42.1
2	41.9
3	40.9

For both three- and six-subcell designs, the carrier lifetime had a dramatic effect on the cell efficiencies, with 1 ns lifetimes producing values more than 13% (absolute) lower than for 10 ns lifetimes. With efficiencies at 1 ns of approximately 20%, the performance was substantially worse than desired for the number of subcells. This is primarily due to the decrease in the number of photogenerated carriers collected as a consequence of the shorter minority carrier diffusion length, though the increase in dark current also contributes. While lifetimes of 1 ns are more realistic for the present status of this materials system [43],[49],[50], simulations with 10 ns lifetimes reflect the potential for enhancing the performance of the cells through future improvements in InGaN materials.

As shown in Tables II.B.2 and II.B.3, increasing the carrier lifetime to 10 ns would enable efficiencies of up to 40% with the present designs, and further optimization could push the performance even higher.

The carrier concentration in the n-type InGaN is important to understanding the strong dependence of the efficiency on carrier lifetime. Carriers generated in the depletion region are quickly separated by drift, making them less likely to be lost due to recombination events than carriers generated in the quasi-neutral region, which must first diffuse to the junction before they can be separated. However, the high electron concentrations typically observed in In-rich InGaN can lead to narrow depletion widths and consequently less efficient charge separation. These simulations assumed an electron concentration of 10^{18} cm^{-3} in the InGaN absorber. As shown in Fig. II.B.2, such a high electron concentration had a detrimental effect on the J_{sc}. Lowering the effective donor concentration to 10^{17} cm^{-3}, as seen in Fig. II.B.2B, broadened the space charge region and caused an increase in J_{sc} of ~4 mA/cm^2. In a hypothetical p-i-n cell structure (Fig. II.B.2C), the space charge region spanned the entire intrinsic region, leading to J_{sc} nearing 100% of the available photocurrent. This confirms that cells with wider space charge regions tend to have higher internal quantum efficiencies. Decreasing the effective donor concentration in the InGaN absorber from 10^{18} cm^{-3} to 10^{16} cm^{-3} mitigated the effects of reduced lifetime, increasing the efficiency of the six-cell design by over 5% (absolute) for the 1 ns case. Thus, the efficiency of any experimental MILAMB cell based on InGaN will depend strongly on both the achievable minority carrier lifetime and effective doping concentration. Nonetheless, with efficiencies exceeding 20% at low concentration ratios for the three-subcell design even with a minority carrier lifetime of 1

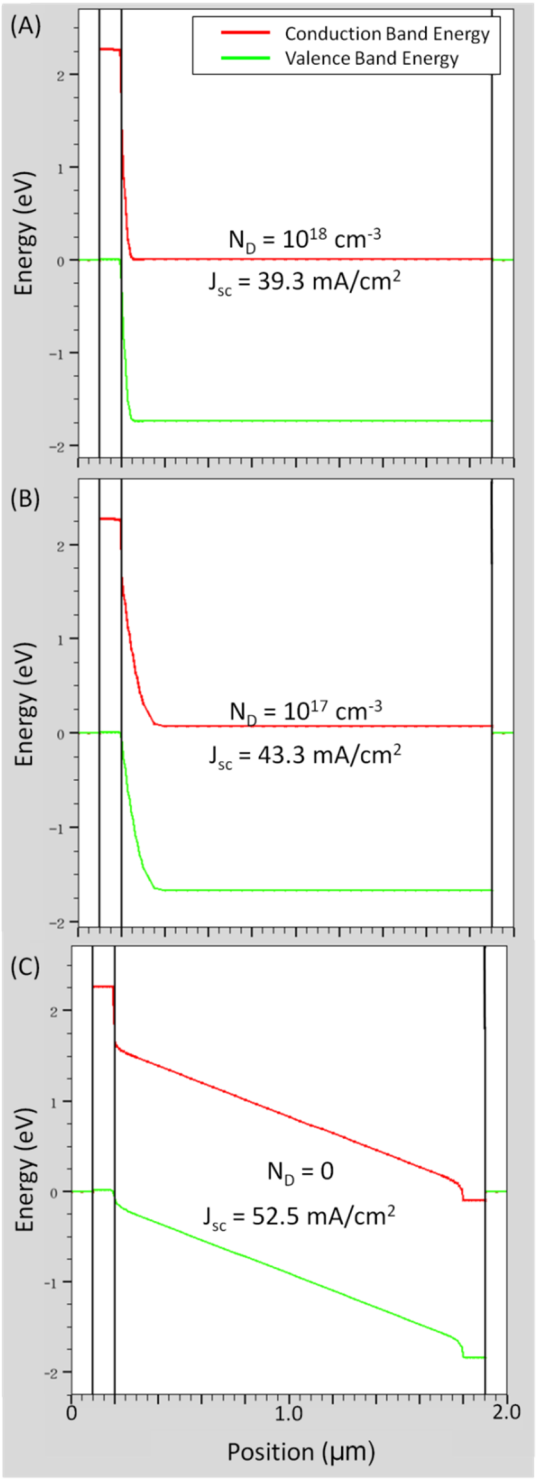

Figure II.B.2: Energy band diagrams for subcell 2 of the six-subcell design with 10 ns carrier lifetimes for (A) $N_D = 10^{18}$ cm^{-3}, (B) $N_D = 10^{17}$ cm^{-3}, and (C) $N_D = 0$ cm^{-3} with a p-i-n cell structure.

ns and effective donor concentration of 10^{18} cm^{-3}, MILAMB solar cells based on InGaN nanowires could be an attractive option for future photovoltaic systems.

II.B.iii. Conclusion

A set of InGaN solar cells for a spectrum-splitting PV system was designed. For six subcells with presently realistic carrier lifetimes of 1 ns, the efficiencies were relatively low given the number of subcells, around 20% at 1 sun AM1.5D illumination and 25% for 240 suns. However, simulations showed that increasing the carrier lifetime to 10 ns dramatically increased the efficiency to 34% and 40% for 1 and 240 suns, respectively. Decreasing the electron concentration in the InGaN absorber from 10^{18} cm^{-3} to 10^{16} cm^{-3} also increased the efficiency by around 5% (absolute) with 1 ns

lifetimes. This suggests the efficiency of any practical system will depend greatly on the achievable carrier lifetimes and electron concentrations in the InGaN nanowires.

II.C. Conclusion

Theoretical design studies were presented for both CdPbS and InGaN MILAMB solar cells. The results showed that both could be potentially attractive options for future implementations of this concept to achieve high efficiencies at low cost. However, in both cases, additional materials work is required before a practical system can be realized. In the case of CdPbS, more research is required to demonstrate alloys spanning the full composition range [33], while for InGaN, In-rich alloys with longer carrier lifetimes or lower electron concentrations are necessary.

In the remaining sections, the design, fabrication, and characterization of CdSe solar cells and proof-of-concept CdSSe solar cells with two subcells using nanowire ensembles and thin films are discussed.

CHAPTER III

CdSSe SOLAR CELLS

As a proof-of-concept demonstration of the MILAMB solar cell concept, with multiple solar cells fabricated in an integrated process using Dual-Gradient CVD, spatially composition-graded CdSSe nanowire ensemble solar cells were fabricated, as detailed in a recent publication [32]. Similar thin film solar cells were also fabricated and served as a useful comparison with these devices. Although the design and simulation studies in the previous chapter were conducted for CdPbS and InGaN, alloys of the desired compositions have not yet been demonstrated in the CdPbS materials system, and InGaN was not available. CdSSe was selected because composition-grading across the full alloy range has been demonstrated [10], and the band gaps available in this system are suitable for at least two subcells (albeit the larger band gap subcells only).

CdS and CdSe are II-VI materials with high absorption coefficients and respective direct energy band gaps of 2.42 and 1.74 eV [42]. Undoped CdS and CdSe both typically display n-type conductivity due to native donors, but are difficult to dope p-type due to heavy compensation effects [38]. Thus, they require a p-type heterojunction partner in order to form a p-n junction to separate photogenerated charge carriers. ZnTe is a p-type semiconductor with a band gap of 2.26 eV [42] which is readily capable of extrinsic p-type doping up to high levels [38]. It has been used as a p-type window layer for CdSe/ZnTe solar cells in literature [55]-[58] and was determined to be the most suitable material for the present application.

In the following sections, the literature on CdSe/ZnTe solar cells is reviewed, and experimental results are presented on the fabrication and characterization of pure CdSe

and CdSSe nanowire ensemble and thin film solar cells with ZnTe as the p-type heterojunction partner.

III.A. Prior Work in Literature

Solar cells based on CdSSe alloys or pure CdS have not been widely studied in literature, excepting devices wherein these materials are not the active layer in the traditional sense (CdS and CdSe quantum-dot sensitized cells have been widely studied). Pure CdSe cells have received somewhat more attention, however, due to the more attractive band gap of this material. The most relevant solar cells in literature to those in this dissertation are CdSe/ZnTe heterojunction cells, which have been investigated by a number of researchers [55]-[58] over the years.

Buch et al. [55] created CdSe/ZnTe solar cells by growing CdSe thin films on ZnTe substrates by close-spaced vapor transport. The CdSe layers were on the order of 1-2 μm thick and had effective net donor concentrations on the order of 10^{16} cm^{-3}, while the ZnTe had hole concentrations of approximately 2 x 10^{17} cm^{-3} [55]. Ohmic contacts to CdSe and ZnTe were made using In and Au, respectively [55]. They estimated that the built-in (or diffusion) potential of the heterojunction was at least 1.27 V and achieved efficiencies and V_{oc}'s as high as 2.52% and 0.68 V, respectively [55]. While these are both the first and the most efficient CdSe/ZnTe solar cells of which this author is aware, ZnTe substrates are expensive and therefore preferably avoided in photovoltaic applications. Later researchers attempted to fabricate similar cells by more cost-effective means.

Nearly two decades later, Patel et al. fabricated a CdSe/ZnTe cell by thermal evaporation of ZnTe and CdSe onto an ITO-coated glass substrate [56]. First, 2 nm of Ag

was deposited directly onto the ITO to catalyze grain growth during the subsequent deposition of a 200 nm layer of ZnTe [56]. Note that Ag also acts as an acceptor in ZnTe, so this method should dope the film p-type [59]. Next, approximately 800 nm of In-doped CdSe was deposited in the same system without breaking vacuum, followed by an In back contact [56]. Built-in potentials as high as 1.42 V were observed, and the efficiency, V_{oc}, and J_{sc} under one-sun illumination were as high as 1.86%, 415 mV, and 11.60 mA/cm^2, respectively [56].

Pal et al. fabricated CdSe/ZnTe thin film solar cells with Cu-doping in the ZnTe layer, much like in the present work [57]. Cells were fabricated on Cr-coated glass substrates, where the Cr served as the back contact [57]. First, 2-3 μm of CdSe was deposited by hot-walled vacuum evaporation in a quartz tube at a substrate temperature of 550 K. Next, 1-1.2 μm of ZnTe was deposited by a similar method at a substrate temperature of 520 K, with Cu doping achieved by co-evaporation of Cu during ZnTe layer deposition [57]. The samples were then annealed at 370 K in Ar for 5 minutes, and Cu-Au contacts were formed on top [57]. They achieved V_{oc} of 480 mV, J_{sc} of 9 mA/cm^2, and 1.3% efficiency.

Most recently, Wang et al. reported fabrication of a single nanowire CdSe/ZnTe solar cell with core-shell structure [58]. To date, this is the only other report of a CdSe nanowire p-n junction solar cell (where the CdSe nanowire(s) comprises the active absorbing layer) of which this author is aware. CdSe nanowires were grown on Si substrates in a quartz tube furnace with Ar/H_2 carrier gas and pure CdSe source powder [58]. Nanowire growth occurred by the vapor-liquid-solid mechanism using Au catalyst [58]. Next, an epitaxial ZnTe shell approximately 20 nm thick was grown by pulsed-laser deposition at a substrate temperature of 350°C [58]. The core-shell CdSe/ZnTe nanowires

were then dispersed on a Si/SiO_2 substrate, and electron beam lithography was used to pattern electrical contacts [58]. The ZnTe shell was contacted by depositing a Ni electrode, and contact to the CdSe core was achieved by etching a portion of the ZnTe shell and depositing In. The best of the resulting devices was reported as having a V_{oc} of 180 mV, I_{sc} of 38 pA, FF of 38%, and approximately 1.3% efficiency under 1 sun illumination [58]. Note that the nanowire growth process was similar to that used in the present work, though simplified compared to the Dual-Gradient Method [11] used to grow CdSSe nanowires. As such, the results obtained by Wang et al. [58] provide a useful comparison to the results obtained here.

Clearly, CdSe/ZnTe solar cells are still relatively undeveloped compared to commercial technologies. The V_{oc} of CdSe thin film cells remains significantly lower than would be expected for mature cells based on the band gap, and as far as this author is aware, Wang et al. [58] represents the only other inorganic p-n junction solar cell with a CdSe nanowire absorber reported in the literature. This context is important to the consideration of composition-graded CdSSe nanowire solar cells fabricated in this work, since they utilize similar materials, but are more complex due to the use of nanowires, alloying with CdS, and spatial composition-grading. Thus, cell performance expectations at this stage were modest, and the primary goal was to demonstrate the fabrication of a novel device with basic operation for proof-of-concept.

III.B. P-type ZnTe Layer Experiments

Prior to fabricating devices, a series of experiments was conducted on the deposition and annealing of Cu-doped ZnTe films, with the goal of achieving a sufficiently high

doping concentration to minimize series resistance, maximize V_{oc}, and enable ohmic contacts to be obtained. ZnTe:Cu films were deposited on glass substrates at ambient temperature by thermal co-evaporation of separate ZnTe and Cu sources in a bell jar system with a base pressure of 2×10^{-6} Torr. The films were approximately 200-300 nm thick, as measured in-situ with a quartz crystal monitor, and consisted predominantly of zincblende ZnTe(111), as characterized by X-Ray diffraction. The sheet resistances of these films were measured by the four point probe technique, both as-grown and following annealing in a tube furnace under a 500 Torr nitrogen atmosphere.

Literature on Cu doping of ZnTe films agrees that Cu incorporation far in excess of the intended doping level is required to achieve high carrier concentrations due to the generation of compensating defects [60],[61]. Typically, doping levels of approximately 6 at.% or more are used to achieve highly p-type ZnTe:Cu films [60]-[62]. The achievable composition control in the present work using the bell jar system was relatively limited, but Cu concentrations during these initial experiments were estimated at roughly 10 at.%.

After growth, the films were annealed to activate the Cu acceptors. To optimize the annealing conditions, a study by Zhang et al. was repeated, wherein the authors deposited ZnTe:Cu films (8 at.% Cu) by thermal co-evaporation and annealed at various temperatures between 144°C and 260°C [62]. The authors found that the conductivities of the films decreased with low temperature annealing, but reached a local minimum and began to increase with progressively higher annealing temperatures [62]. They explained this behavior using a theory developed by John Seto in a 1975 paper [63] on electrical conduction in polycrystalline silicon films. Seto argued that trap states at grain

boundaries caused the film conductivity to vary with doping in an unexpected manner [62],[63]. When the number of activated dopants is less than the number of trap states, the grains are essentially depleted of carriers, and increasing the doping concentration simply fills these trap states with the charge carriers contributed by doping [62],[63]. This causes potential barriers to form at the grain boundaries, the height of which are proportional to the number of activated dopants, hindering conduction between grains and effectively reducing the carrier mobilities [62],[63]. However, when the number of activated dopants exceeds the number of trap states, the potential barrier heights decrease as the inverse of the doping concentration and conductivity increases [62],[63]. When Cu-doped ZnTe films are annealed at increasingly higher temperatures, more of the dopants are activated and this pattern of doping-dependent conductivity is observed [62].

Fig. III.B.1 shows the resistivity of a single ZnTe:Cu film after subsequent anneals, each conducted for one hour in a nitrogen atmosphere. The as-grown film had a fairly high conductivity which was never fully recovered during the annealing process. It experienced a dramatic rise in resistivity after the first anneal at 144°C, but subsequent annealing brought the resistivity back down, reaching a local minimum after annealing at approximately 220°C. This is similar to the study by Zhang et al., where the films were optimized at 260°C, however they did not present any data on higher annealing temperatures [62]. In the present work, annealing above 260°C caused the resistivity to increase rapidly, the cause of which remains unknown. Nonetheless, the local minimum in resistivity indicates successful doping of ZnTe films with Cu was achieved with annealing at 220°C.

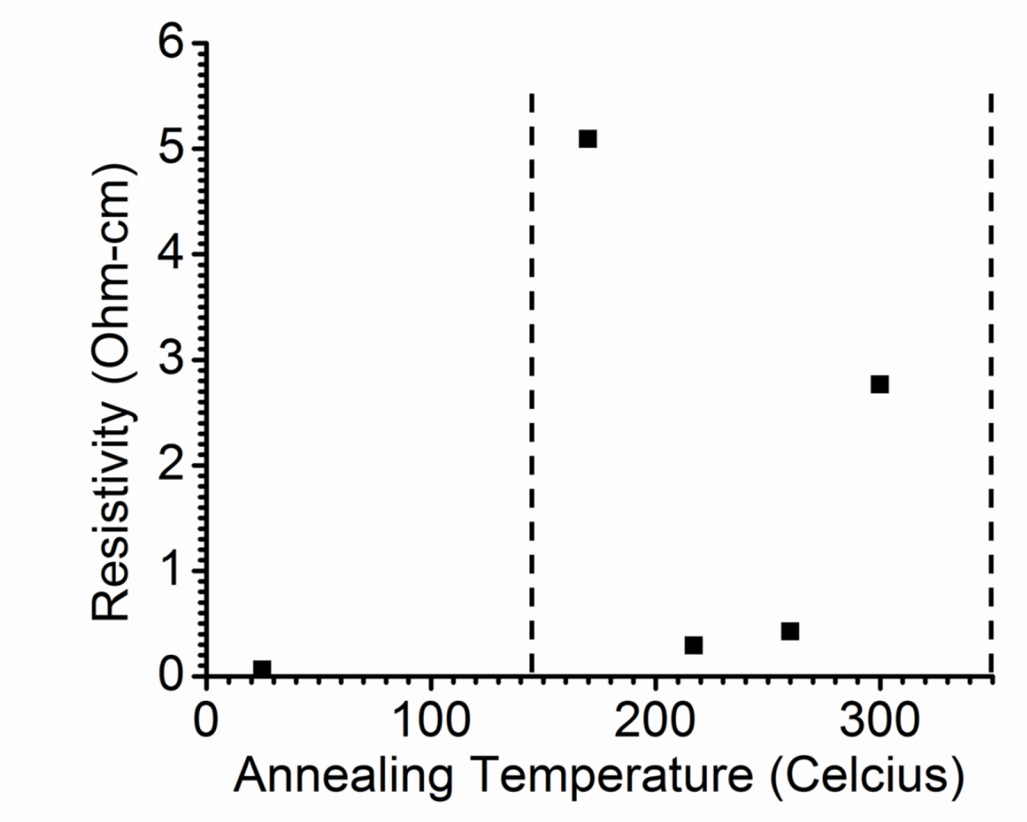

Figure III.B.1: Resistivity of ZnTe:Cu deposited at ambient temperature by thermal co-evaporation versus annealing temperature; vertical dotted-lines indicate that the sheet resistance was too large to measure with the four-point probe.

A precise measurement of the hole concentration by the Hall technique was not performed. However, Tang, Mao, and Trefny found the hole mobilities in ZnTe films prepared by a similar method with Cu concentrations of 6-8 at.% to be roughly 1 cm^2/Vs [60]. Assuming similar mobilities were obtained in the present work, the acceptor concentration of the sample in Fig. III.B.1 after annealing at 220˚C was estimated to be over 10^{19} cm^{-3}, which is sufficiently high for the present application.

However, it was necessary to use far lower Cu content (~1 at.%) during the fabrication of complete devices in order to prevent device instability and improve performance. Thus, the effective doping levels in the ZnTe window layers used for cell fabrication are

anticipated to be lower than those achieved in these preliminary experiments. Nonetheless, the determination of 220°C as the optimum temperature for activating Cu acceptors in ZnTe was crucial for device fabrication.

III.C. Pure CdSe Solar Cells

Pure CdSe nanowire ensemble and thin film solar cells were fabricated in order to tune the fabrication process for the more complicated two-subcell devices based on spatially composition-graded CdSSe alloys, as well as for comparison with their performance. In the long term, nanowire cells are preferred due to the potential of nanowires grown by the Dual-Gradient method to achieve better crystal quality than corresponding thin films. However, the challenges associated with fabricating large-area nanowire-based devices are significant. As discussed later in this section, misalignment of the nanowires led to reduced J_{sc}'s due to problems contacting all of the wires. Thus, it was useful to fabricate thin film devices in addition to nanowire ensemble cells for comparison. The fabrication and characterization of CdSe nanowire and thin film solar cells are discussed in the following sections.

The CdSe film cells demonstrated superior performance to the nanowire cells, with V_{oc} and J_{sc} up to 381 mV and 2.560 mA/cm^2, as compared to 188 mV and 0.527 mA/cm^2 for the nanowire cells. Fill factors were also higher for the film cells, albeit still poor, with values up to 37%, as compared to less than 29% for the nanowire cells. The lower V_{oc} and FF in the nanowire cells was attributed to shorter carrier lifetimes in the nanowires due to surface recombination. Lower J_{sc} in the nanowire cells was attributed both to shorter carrier lifetimes and to spin-on glass burying some of the nanowires.

Comparison between these cells and the two-subcell CdSSe devices was also performed and is discussed later in this dissertation.

III.C.i. CdSe Nanowire Solar Cell Fabrication

Two generations of CdSe nanowire solar cells were fabricated in this work. The key difference between the two was the choice of interlayer dielectric material, as will be discussed later in more detail. Their layer structures are shown in Fig. III.C.1.

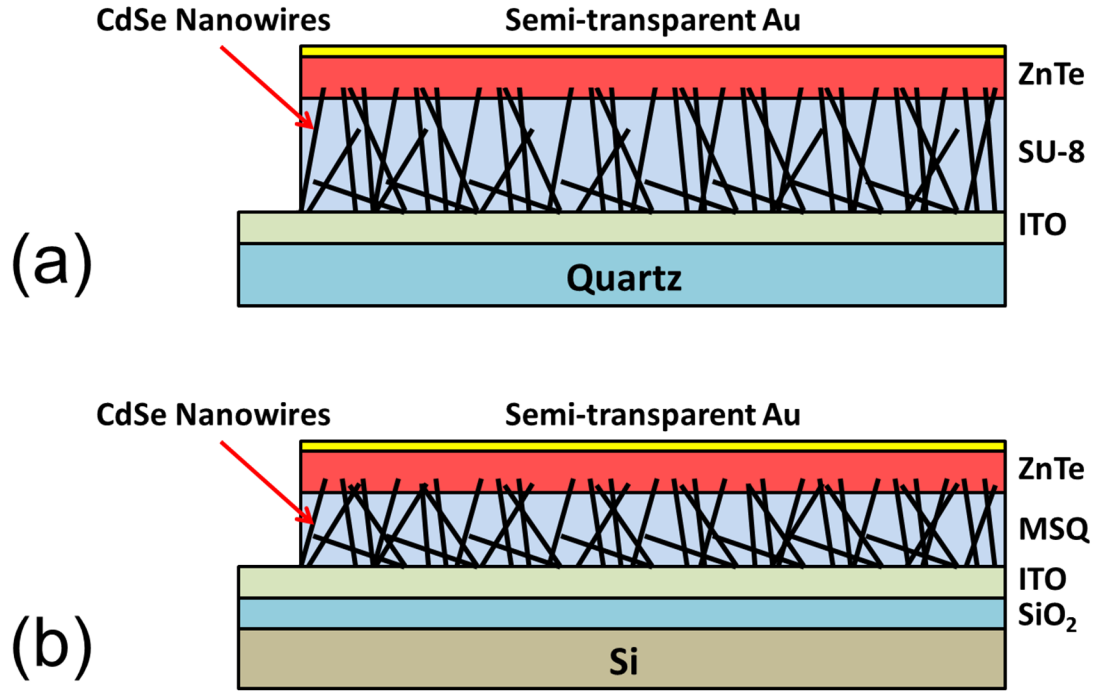

Figure III.C.1: CdSe nanowire solar cell structures for (a) early devices using SU-8 as an interlayer dielectric and (b) later devices using thinner methylsilsesquioxane (MSQ).

The first generation of CdSe nanowire ensemble solar cells (Fig. III.C.1a) was fabricated as follows. First, 100-200 nm of ITO was sputtered onto a quartz substrate. A thin Au film approximately 11-13 nm thick was sputtered on top as the catalyst material for vapor-liquid-solid (VLS) growth of CdSe nanowires. Next CdSe nanowires were grown by CVD in a tube furnace using electronic grade (99.99% pure) CdSe source

powder and Ar with 5% H_2 by mole fraction carrier gas. The source temperature was 900°C, and the substrate temperature was approximately 500°C at the leading (upstream) edge, with the substrate itself oriented horizontally in the tube. The source temperature was gradually ramped to 900°C over a period of 20 minutes and held constant at this value for one hour. The Ar/H_2 volume flow rate was 50 sccm, and the pressure during growth was held at 15 ± 1 Torr. Fig. III.C.2 shows a representative SEM image of the resulting CdSe nanowires. They were typically quite long, often exceeding 10 μm in length, and tended to display a flat, tapered morphology which was termed nanobelts.

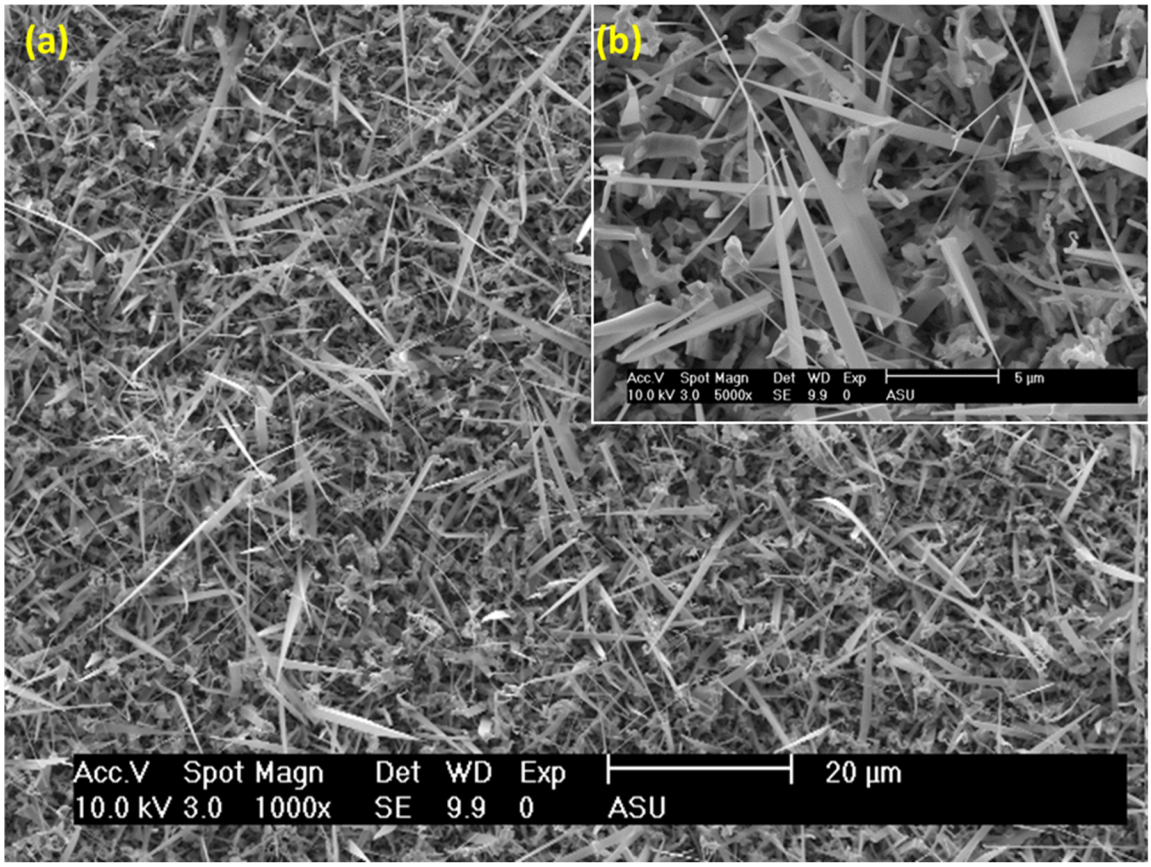

Figure III.C.2: SEM images of CdSe nanobelts resulting from a 30 min growth on a quartz/ITO substrate under a) 1000x magnification and b) 5000x magnification.

Next, SU-8 photoresist was applied by spin-coating to fill-in the gaps between nanowires and prevent shorting with the ITO after p-ZnTe deposition. The thickness of

the SU-8 layer on a bare substrate was approximately 7-8 μm, as measured by profilometry, but this increased to roughly 12 μm when applied to a nanowire ensemble. A flood exposure was performed to cross-link the resist, after which it was hard-baked up to 250°C on a hot plate in air to prevent further shrinkage during later high temperature processing. During this step, the hot plate was ramped slowly from 65°C up to 250°C to prevent delamination of the SU-8 from the substrate due to the accumulation of stress in the film. The CdSe nanowires protruding from the SU-8 (shown in Fig. III.C.3) were planarized by rubbing the surface of the sample with an abrasive cloth or piece of soft, textured paper. This was performed to obtain a more level surface for the deposition of the p-ZnTe window layer without scratching the SU-8.

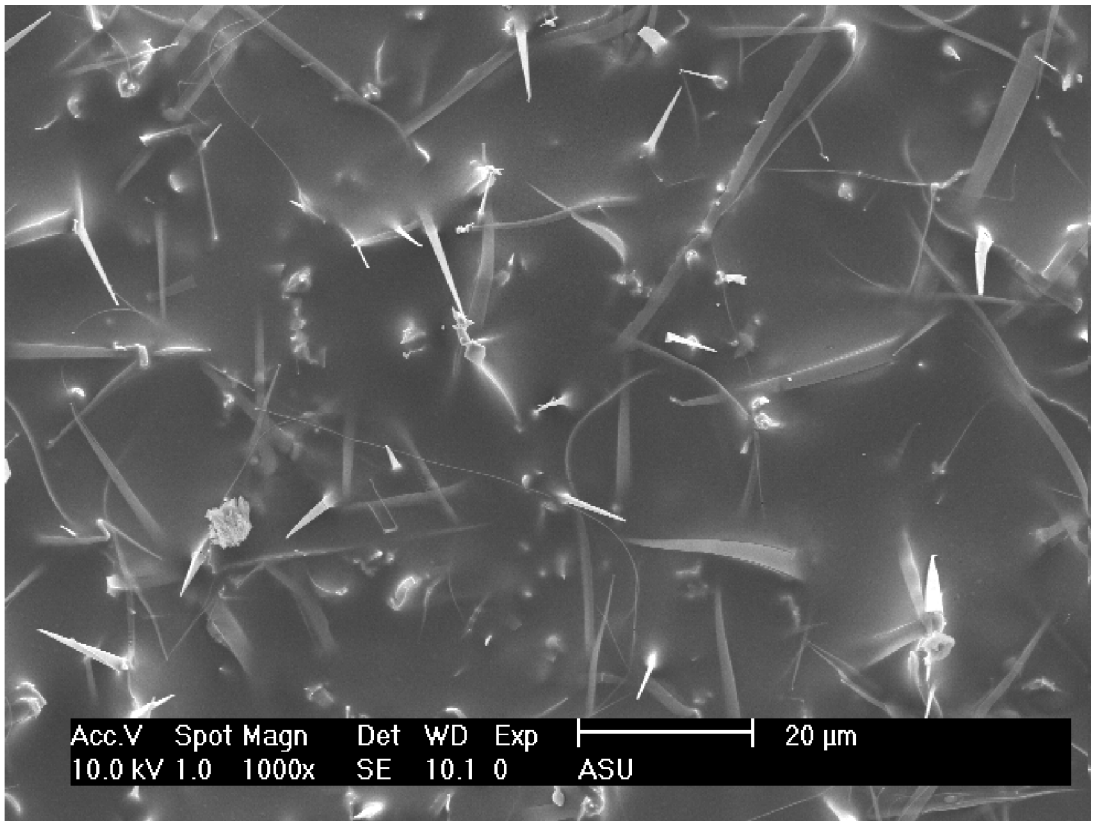

Figure III.C.3: CdSe nanobelts after spin-coating with SU-8 [32].

To form the ZnTe:Cu window layer, roughly 150-300 nm of ZnTe and 2 nm of Cu were deposited sequentially by thermal evaporation with the substrate at ambient temperature. A thin layer of Au approximately 11-13 nm thick was then sputtered on top as a semi-transparent contact (~40% transparent in the 500-900 nm wavelength range). The sample was then annealed in a 400-500 Torr nitrogen atmosphere at 220°C for one hour to increase the grain size of ZnTe and activate the Cu acceptors. X-ray diffraction results indicate that the grain size of the dominant zincblende (111) orientation increased from approximately 25-30 nm to 50-60 nm during this step. The final device structure is shown schematically in Fig. III.C.1a.

For the second generation of CdSe nanowire solar cells (Fig. III.C.1b), a number of refinements were made to the fabrication process. Firstly, the quartz substrate was replaced by Si(100) with 400 nm of SiO_2 deposited by plasma-enhanced chemical vapor deposition (PECVD). This facilitated more controlled substrate cleaving, which allowed for greater standardization of substrate sizes and shapes. Nanowire growth was performed with the substrates oriented vertically, rather than horizontally as for earlier devices. Combined with the greater thermal conductivity of Si(100), this helped to create a more uniform vapor-phase supersaturation over the substrate surface during growth, which dramatically improved growth uniformity and sample coverage. The growth recipe itself was also changed. The CdSe source temperature was decreased from 900˚C to 700˚C, the substrate temperature was increased to 620˚C, the pressure was decreased to 5.0 ± 0.1 Torr, and the Ar/H_2 flow rate was increased to 100 sccm. These conditions gave more repeatable results, likely due to more consistent substrate temperatures facilitated by the more gradual temperature gradients at lower furnace temperatures.

The most important modification was the replacement of SU-8 with a thinner interlayer dielectric, methylsilsesquioxane (MSQ). As shown in Fig. III.C.3, only a small percentage of the CdSe nanowires protruded from the SU-8 in early devices. As will be shown later, this resulted in J_{sc} that was three or more orders of magnitude lower than comparable film cells. Methylsilsesquioxane spin-on glass was found to form layers approximately 500-600 nm thick when applied to a bare substrate and roughly 4 μm thick in a nanowire ensemble, as measured by profilometry and cross-sectional SEM (Fig. III.C.4). Comparing the nanowire ensemble with MSQ in Fig. III.C.4 to that with SU-8 in Fig. III.C.3, it is clear than many more nanowires protrude through the dielectric layer in the case of MSQ. It is shown later that this dramatically improved the J_{sc}, though most devices still fell somewhat short of comparable film cells in this respect.

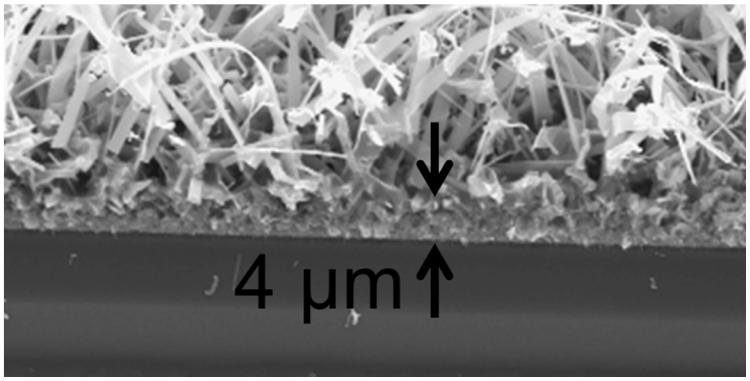

Figure III.C.4. Cross-sectional SEM image of a CdSSe NW ensemble after MSQ application [32]. The MSQ layer is found to be approximately 4 μm thick.

Finally, ZnTe and Cu were deposited at a substrate temperature of 220˚C using a heated sample stage, rather than depositing at ambient temperature and annealing. This simplified the fabrication process and is anticipated to have improved the quality of the ZnTe layer, however no significant improvement in device performance was identified.

III.C.ii. CdSe Thin Film Solar Cell Fabrication

The fabrication process for CdSe thin film solar cells is outlined in Fig. III.C.5 below. It is similar to that for the nanowire cells, but differs in several respects. The growth of CdSe films followed a similar process to that for nanowires, however no Au catalyst was used. CdSe films approximately 5-7 μm thick were deposited by CVD at a source temperature of 700˚C with Ar/H_2 carrier gas flowing at 100 sccm. The furnace was gradually heated to 700˚C over 20 min and held for a growth time of one hour, during which the system pressure and substrate temperature were 5.0 ± 0.1 Torr and 500-550˚C, respectively. The spin-on dielectric application and planarization steps used for the nanowire cells were not required for a continuous film, so these were omitted. All other steps were identical to those used for the nanowire cells.

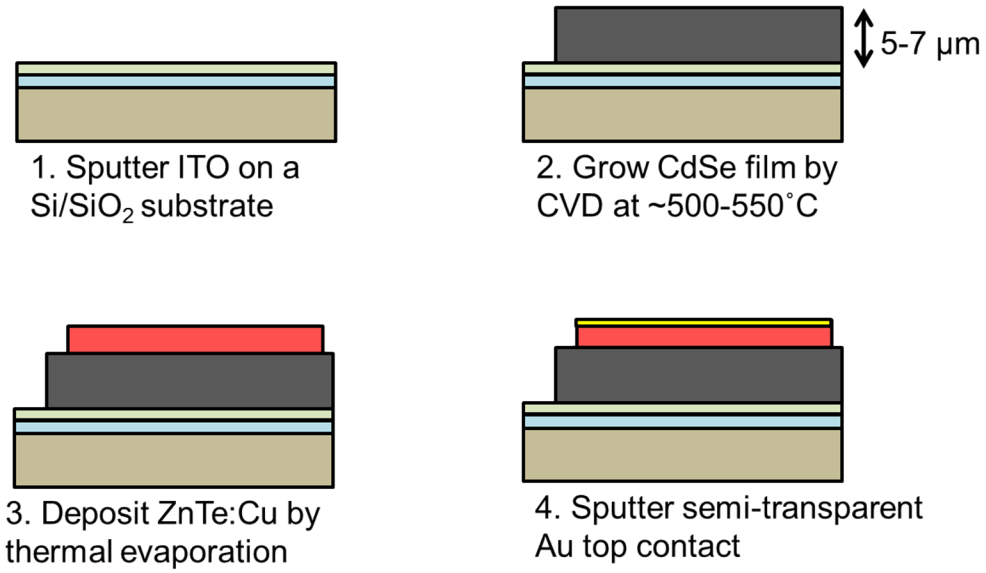

Figure III.C.5: Fabrication process for CdSe thin film solar cells.

III.C.iii. Au Top Contact Transmission

Before examining the I-V performance of the cells in this work, it is first necessary to consider the efficiency with which photons are coupled into the cell through the thin Au top contact. The optical transmission of the Au top contact was characterized by comparing the intensities of light transmitted through quartz samples with and without the thin Au layer using an integrating sphere. A layer of Au approximately 11-13 nm thick was sputtered onto a bare quartz substrate, which was then placed at the admitting aperture of the sphere. A halogen lamp was used to illuminate the sample, such that the transmitted photons entered the sphere and were detected. The experiment was then repeated with a bare quartz substrate. Dividing the intensity of the detected signal for the Au-coated sample by that for the bare quartz gave the optical transmission as a function of wavelength, which was found to be approximately 40% between 500 and 900 nm, as shown in Fig. III.C.6. This is comparable to the transparency of a very similar top contact in literature consisting of 1 nm Cu and 13 nm Au, which was found to be in the 40-60% range for wavelengths of 500-900 nm [64]. Note that this contact structure was selected for the proof-of-concept devices in this work due to its simplicity, and a mature cell design would utilize a top contact structure with much higher transmission, leading to a corresponding increase in cell currents. The short-circuit currents reported in this work should therefore be interpreted relative to the opacity of the top contact.

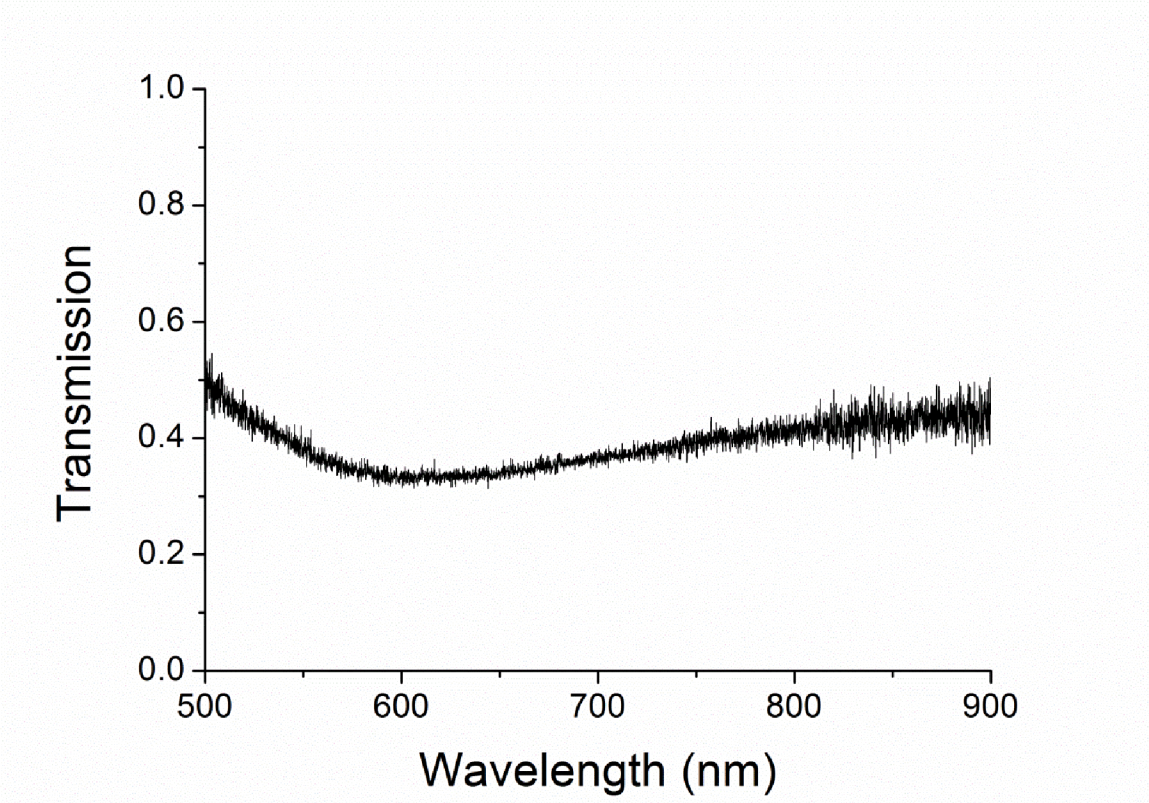

Figure III.C.6: Optical transmission of an 11-13 nm thick sputtered Au top contact, as measured using an integrating sphere [32].

III.C.iv. CdSe Nanowire Solar Cell Results

The cells fabricated in this work were first evaluated by probing the I-V characteristics under illumination by a halogen lamp. Those that demonstrated sufficient performance were measured under more realistic conditions using a solar simulator.

The I-V characteristics of the first generation of CdSe nanowire solar cells, which were fabricated using SU-8 as an interlayer dielectric, were measured under illumination by a halogen lamp at 13.2 mW/cm^2 using a Keithley 6487 picoammeter. The performance of these cells is summarized in Table III.C.1, and the I-V characteristics of a representative device are shown in Fig. III.C.7. V_{oc} up to 188 mV was obtained, which is

comparable to that achieved for a single nanowire CdSe solar cell under higher intensity 1 sun AM1.5G conditions by Wang et al. [58]. However, I_{sc} for these devices was on the order of nA, which is roughly five orders of magnitude below expectations for cells with active areas on the order of 1 cm^2 under these illumination conditions. This is due to the relatively thick (~12 μm) SU-8 layer and unaligned nature of the nanowire ensemble, which caused the majority of wires to be entirely submerged in the SU-8, as shown in Fig. III.C.3. Thus, only a small number of nanowires were in contact with the ZnTe layer to form active p-n junctions in the device. Photogenerated carriers in uncontacted wires could not be separated and were lost, effectively rendering the majority of the device area inactive. Due to their low I_{sc}'s, these cells were not measured under AM1.5G conditions.

Table III.C.1: I-V performance properties of CdSe nanowire cells fabricated using SU-8 under illumination by a 13.2 mW/cm^2 halogen lamp.

Sample ID	**V_{oc} (mV)**	**I_{sc} (nA)**	**FF**
10242012D	188	0.26	28.4%
01112013D	172	9.04	25.6%
01112013E	126	4.08	26.5%
09192012E	22	3.40	25.3%

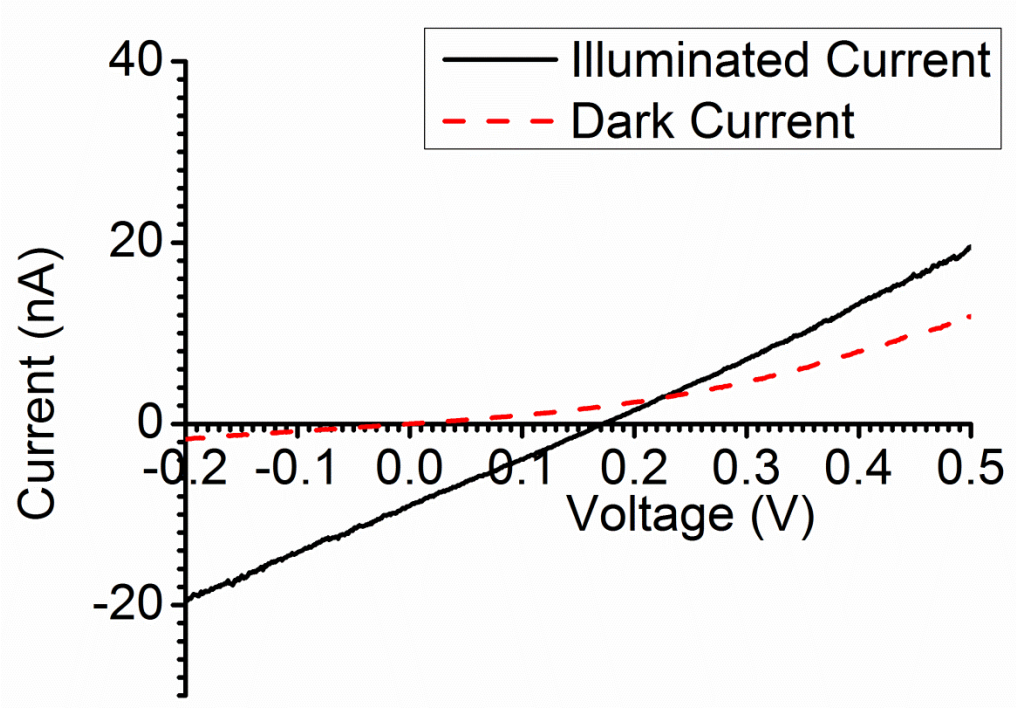

Figure III.C.7: I-V characteristics of a first-generation CdSe nanowire solar cell (01112013D) with SU-8 as the interlayer dielectric under 13.2 mW/cm^2 halogen lamp illumination and in the dark.

To increase the number of nanowires in contact with the ZnTe layer, the second generation of CdSe solar cells was fabricated with MSQ as the interlayer dielectric instead of SU-8. MSQ formed a thinner layer than SU-8, approximately 4 μm instead of 12 μm, so a far greater number of nanowires protruded from the dielectric layer, as seen by cross-sectional SEM in Fig. III.C.4. Thus, a far greater number of nanowires were in contact with the ZnTe layer in the second generation of CdSe nanowire cells, and this lead to a dramatic increase in photocurrent.

I-V characterization of second-generation CdSe nanowire ensemble solar cells fabricated with MSQ was conducted under 1 sun AM1.5G conditions using an Oriel Class A solar simulator and Keithley 2420 source meter. The cells were mounted on glass

stages with Au electrodes. Wire-bonding was performed using Au wires and conductive Ag epoxy. A 4 mm diameter aperture was placed over the cells to define an active illuminated area for calculating the current density, and the cell current was observed while sweeping the voltage. The performance of these cells is summarized in Table III.C.2, and the dark and illuminated I-V characteristics of a representative device are shown in Fig. III.C.8.

Table III.C.2: I-V performance properties of CdSe nanowire solar cells fabricated using MSQ under 1 sun AM1.5G illumination conditions.

Sample ID	**V_{oc} (mV)**	**J_{sc} (mA/cm^2)**	**FF**
02192014Q	88	0.433	26.8%
02192014R	71	0.527	26.1%
02192014S	14	0.183	24.8%
02192014T	61	0.331	26.9%

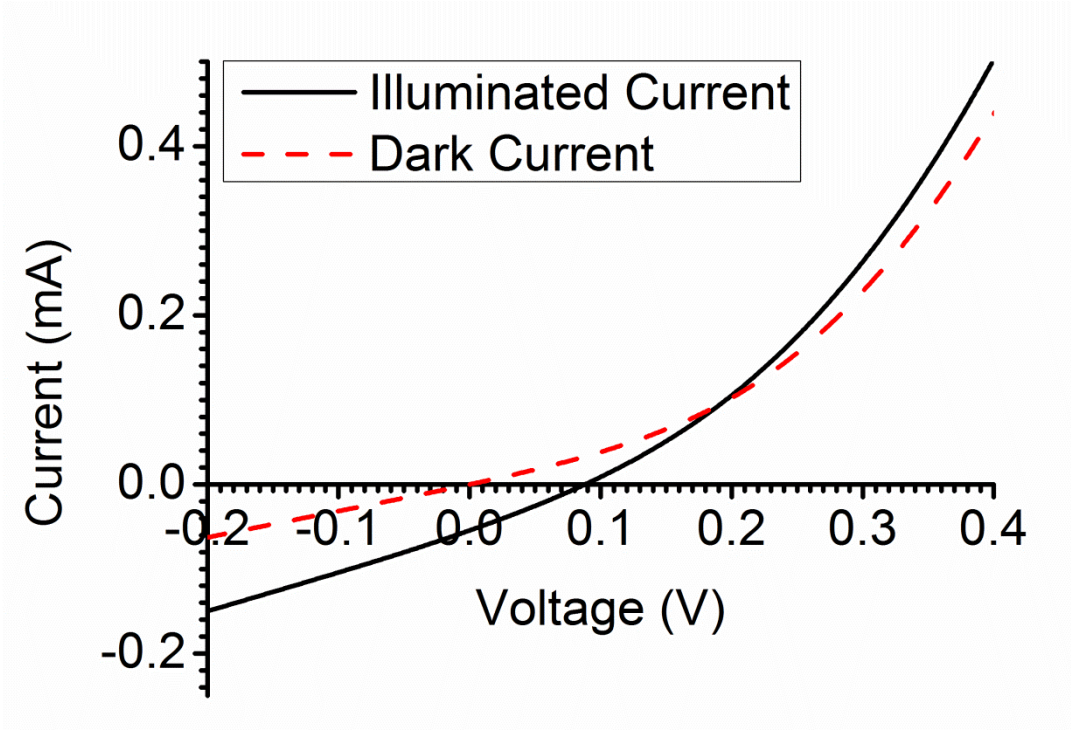

Figure III.C.8: I-V characteristics of a second-generation CdSe nanowire solar cell (02192014Q) with MSQ as the interlayer dielectric under 1 sun AM1.5G illumination through a 4 mm diameter aperture and in the dark.

V_{oc} was relatively modest for these cells, up to 88 mV under AM1.5G conditions. While these results cannot be directly compared to the cells fabricated using SU-8 due to the different illumination spectra and intensities, it is nonetheless clear that J_{sc} is dramatically higher than in those earlier devices, while V_{oc} is somewhat lower. The simultaneous observation of dramatically increased J_{sc} and reduced V_{oc} is indicative of contacting a much greater number of nanowires. In a typical solar cell, the V_{oc} increases logarithmically with J_{sc}. However, the measured J_{sc} in these cells is simply I_{sc} divided by the illuminated area, which contains both contacted and uncontacted wires. It is therefore an average over both active and inactive regions of the cell. The V_{oc} is related to the J_{sc} within individual nanowires, which is not increased by contacting additional wires. Thus, dramatically increasing the number of nanowires that are contacted should cause a dramatic increase in measured J_{sc} without a noticeable change in V_{oc}, in agreement with experimental observations.

Nonetheless, J_{sc} still fell somewhat short of expectations for an ideal CdSe cell. Assuming full absorption of incident light and accounting for the 40% transparency of the top contact, the maximum potential J_{sc} is predicted to be approximately 8.6 mA/cm^2 under 1 sun AM1.5G illumination. However, the actual values achieved in Table III.C.2 have an average of approximately 0.37 mA/cm^2, a discrepancy of roughly 20 times. This is believed to be due to a combination of two effects. Firstly, it is anticipated that some of the nanowires are still submerged in the dielectric layer, even after switching from SU-8 to MSQ. Secondly, short carrier lifetimes (approximately 0.4 ns, as measured by time-correlated single photon counting) in the CdSe nanowires due to recombination at surfaces and defect levels lead to bias-dependent carrier collection, which reduced the

carrier collection efficiency, and therefore J_{sc} and V_{oc}. This effect is discussed in detail in a later section. To determine the relative importance of these two effects, it is helpful to examine the CdSe thin film solar cells in this work, as they were fabricated in a very similar process but did not have a spin-on dielectric layer. They are discussed in the following section.

III.C.v. CdSe Thin Film Solar Cell Results

The I-V characteristics of CdSe thin film solar cells were measured under 1 sun AM1.5G conditions in a similar manner to the CdSe nanowire ensemble cells. Their I-V performance parameters are listed in Table III.C.3, and the dark and illuminated I-V curves of a representative device are shown in Fig. III.C.9. The CdSe thin film cells achieved significantly better performance than the nanowire cells, with V_{oc} and J_{sc} as high as 381 mV and 2.560 mA/cm^2, respectively. Fill factors were somewhat better than the CdSe nanowire cells as well, though still relatively poor. The higher V_{oc} and FF of the film cells are believed to be due to longer carrier lifetimes. Time-correlated single photon counting found the carrier recombination lifetime to be approximately 0.8 ns in the films, as compared with just 0.4 ns in the nanowires, which likely suffered from greater surface recombination. The longer carrier lifetimes also contributed to the higher J_{sc} of the film cells, which averaged approximately four times larger than in the nanowire cells, although the greater ease of forming a junction with ZnTe for the films was also a major factor. As will be discussed in the following section, the dependence of carrier collection efficiency on recombination lifetime is predicted to be approximately linear in these cells. Thus, lifetimes in the films measuring twice those in the nanowires account for roughly

half of the fourfold difference in J_{sc} between the two types of cells. The remainder is believed to be related to spin-on glass burying some nanowires.

Table III.C.3: CdSe thin film solar cell I-V performance parameters under 1 sun AM1.5G illumination.

Sample ID	**V_{oc} (mV)**	**J_{sc} (mA/cm^2)**	**FF**
05222013X	381	0.782	33.4%
08272013A	280	1.129	28.9%
08272013K	249	1.199	24.5%
08272013E	120	2.139	37.0%
08272013H	96	2.560	27.9%

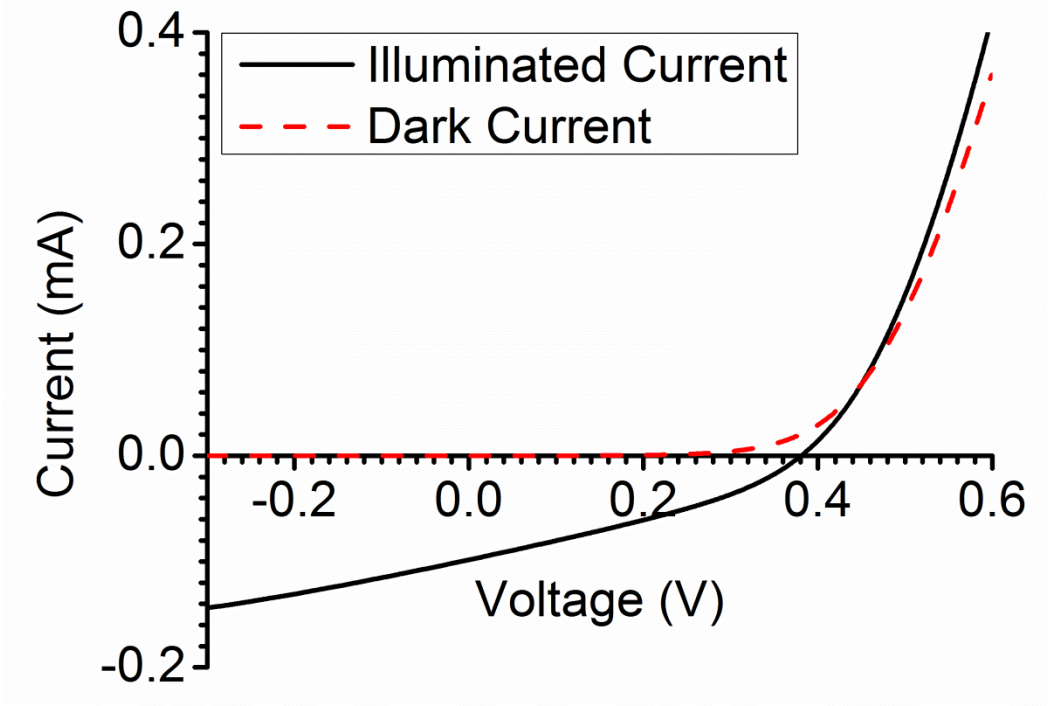

Figure III.C.9: I-V curves of a CdSe thin film solar cell (05222013X) in the dark and under 1 sun AM1.5G illumination through a 4 mm diameter aperture.

Comparing the CdSe thin film cells fabricated in this dissertation to those in literature (reviewed in section III.A), it is found that the best V_{oc} of 381 mV approaches those of some cells fabricated in literature, such as the 415 mV result achieved by Patel et al. [56]. However, the V_{oc}'s are somewhat lower on average. This can be partly attributed to the opacity of the semi-transparent Au contact. Since 60% of incident photons never reach

the active region, the V_{oc} is expected to suffer a penalty of almost 50 mV (assuming an ideality factor n = 2, as appropriate when the photocurrent is dominated by absorption in the depletion region) [15]. This can account for the V_{oc} performance gap with Patel et al. [56], however researchers who achieved higher V_{oc} likely had somewhat higher quality materials and interfaces. This was certainly the case for Buch et al. [55], where the CdSe films were deposited directly on ZnTe substrates with presumably higher quality than the thermally evaporated ZnTe films in this dissertation. Interestingly, however, the J_{sc}'s achieved by Buch et al. were only slightly higher on average than those in this dissertation, despite the opacity of the Au top contact. The J_{sc}'s reported by other researchers [56],[57] were substantially larger, however. Overall, comparison with literature suggests that the CdSe film cells fabricated here approached the level of performance seen in literature in some cases, but tended to be slightly lower.

III.C.vi. Bias-Dependent Carrier Collection

For reverse-bias and small forward-bias voltages, the currents in many of the cells in this dissertation were essentially linear with voltage. However, this was not observed in the dark I-V curves, which tended to display more conventional rectifying diode behavior. The contrast between light and dark I-V behavior can be seen most clearly in Fig. III.C.9 and indicates that the linear I-V responses in the illuminated curves were not caused by shunts. Rather, this is characteristic of a phenomenon known as bias-dependent carrier collection, which is often observed in thin film solar cells. Due to the short diffusion lengths in these cells, essentially all output current is attributable to carriers generated in the space charge region, where the presence of an electric field allows

charges to be quickly separated and collected [65]. However, for very short carrier recombination lifetimes comparable to the time required for carriers to drift to the edge of the depletion region, there is a significant probability of recombination before collection [65]. The drift time is inversely related to the magnitude of the electric field, which is larger for smaller forward-bias or larger reverse-bias voltages [65]. Longer drift times result in higher recombination losses and, consequently, lower current [65].

The collection probability for p-i-n solar cells can be described as follows, though the result has been found to fit polycrystalline thin film cells in general [65]. Assuming a uniform field in the depletion region, as in the intrinsic region of a p-i-n junction, the drift time τ_D is given by:

$$\tau_D = \frac{W}{\mu E} = \frac{W^2}{\mu(V_0 - V)}, \tag{III.1}$$

where W is the distance carriers must drift to be collected and is on the order of the depletion width, μ is the carrier mobility, V is the voltage, and V_0 is a parameter of the cell less than the built-in potential [65]. The collection probability for carriers generated in the depletion region is [65]:

$$\eta_C = 1 - \exp\left(-\frac{\tau_R}{\tau_D}\right). \tag{III.2}$$

Substituting equation (III.1) into equation (III.2) gives:

$$\eta_C = 1 - \exp\left(-\frac{\tau_R \mu}{W^2}(V_0 - V)\right). \tag{III.3}$$

For short recombination lifetimes ($\tau_R < \tau_D$), the exponential can be approximated by a first order expansion, giving:

$$\eta_C \approx \frac{\tau_R \mu}{W^2}(V_0 - V). \quad \text{(III.4)}$$

Thus, under the above assumptions, the carrier collection probability decreases linearly with voltage, leading to a linear I-V relationship at low voltages (where forward-diode diffusion current is negligible) under illumination. Note that this case is distinguishable from a shunt in that linear I-V behavior is not observed in the dark, where there are no photogenerated carriers to collect.

The CdSe thin film solar cell I-V characteristics shown in Fig. III.C.9 clearly fit the bias-dependent carrier collection model. The illuminated I-V curve is linear at lower voltages, whereas the dark curve shows more typical diode behavior (ruling out shunting as the cause). Moreover, time-resolved photoluminescence measurements of as-grown CdSe films showed carrier recombination lifetimes of approximately 0.8 ns. The drift times in these cells are unknown and depend on the hole mobilities in the polycrystalline CdSe films, the equilibrium carrier concentrations in the CdSe and ZnTe films, and other factors such as the band offset which may affect V_0. However, assuming reasonable values of W = 1 μm, μ_p = 5 cm^2/Vs, and V_0 = 1 V, the anticipated drift times from equation (III.1) are 2 ns at V = 0 V and 4 ns at V = 0.5 V. This suggests that bias-dependent carrier collection is expected to occur for measured carrier lifetimes of 0.8 ns, confirming the plausibility of this explanation for the I-V behavior observed in these and other cells in this dissertation.

III.C.vii. Conclusion

Pure CdSe nanowire ensemble and thin film solar cells were fabricated with Cu-doped ZnTe as the p-type heterojunction partner. Early CdSe nanowire solar cells fabricated using SU-8 achieved V_{oc} up to 188 mV under 13.2 mW/cm^2 halogen lamp illumination, on par with a recently reported single nanowire CdSe solar cell under higher intensity, 1 sun AM1.5G illumination [58]. However, the J_{sc} of these cells was extremely small, on the order of nA, due to the relatively thick SU-8 polymer layer (~12 μm) burying many nanowires. Replacing SU-8 with thinner MSQ led to a dramatic increase in J_{sc}, and subsequent cells achieved values up to 0.527 mA/cm^2 under 1 sun AM1.5G illumination, though V_{oc} was more modest at up to 88 mV. For the thin film cells, open-circuit voltages as large as 381 mV were obtained, approaching some prior CdSe/ZnTe cells in literature, albeit somewhat lower [55]-[57]. The difference in V_{oc} between the nanowire and film cells was attributed to shorter carrier lifetimes in the nanowires, approximately 0.4 ns as compared to 0.8 ns in the films, likely due to higher surface recombination. This also accounted for approximately half of the fourfold difference in J_{sc} between the film and nanowire cells due to lower carrier collection efficiency in the nanowire cells. The remainder was attributed to MSQ covering a portion of the nanowires. In the following sections, the knowledge acquired from the pure CdSe nanowire and thin film solar cells was applied to demonstrate proof-of-concept composition-graded CdSSe nanowire solar cells with two subcells.

III.D. Spatially Composition-Graded CdSSe Two-Subcell Devices

Next, spatially composition-graded CdSSe nanowire ensemble solar cells with two subcells were fabricated simultaneously on the same substrate as a proof-of-concept demonstration of a MILAMB solar cell, as detailed in a recent publication [32]. The structure of these devices is shown schematically in Fig. III.D.1. I-V characterization was performed under 1 sun AM1.5G conditions, both with and without optical filters, which were used to simulate spectrum-splitting and observe the performance of both subcells at similar levels of above-band gap photon flux. Similar composition-graded thin film cells were also fabricated for comparison. Unlike the pure CdSe solar cells, the nanowire cells in this case demonstrated significantly higher V_{oc} than their thin film counterparts. The CdS- and CdSe-rich nanowire ensemble cells demonstrated V_{oc} up to 307 and 173 mV and J_{sc} up to 0.091 and 0.974 mA/cm^2, respectively. I-V measurements under filtered illumination, with both subcells receiving similar levels of above-band gap photon flux, showed that the CdS-rich cells achieved uniformly higher V_{oc} and FF than the corresponding CdSe-rich cells, as expected due to their larger band gaps. This suggests that if all nanowires can be contacted and the subcells optimized for current-matching, the larger band gap CdS-rich cell should produce more power than the smaller band gap CdSe-rich cell, which is the key benefit of spectrum-splitting that enables high efficiencies to be obtained. This constitutes a proof-of-concept demonstration of a MILAMB solar cell. Although the performance at this stage and with the present materials was modest, this approach to fabricating multiple cells for spectrum-splitting PV systems in an integrated process on one substrate could offer a low cost alternative to traditional multi-junction tandems for achieving high efficiencies.

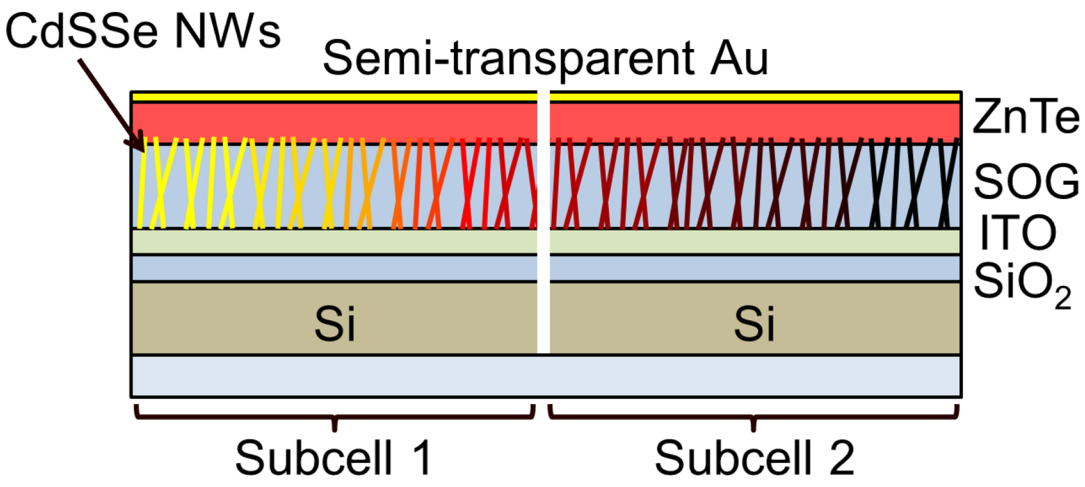

Figure III.D.1: Layer structure of the proof-of-concept MILAMB solar cells based on spatially composition-graded CdSSe nanowire ensembles [32].

III.D.i. Fabrication

The fabrication processes for the CdSSe cells were similar to those for the pure CdSe thin film and nanowire ensemble cells, with two notable changes: 1) the CdSe film or nanowire growth was replaced with spatially composition-graded CdSSe growth; 2) after fabricating the cell structure, the samples were cleaved to create two separate subcells. These modifications are discussed below, and the entire fabrication process is summarized in Fig. III.D.2.

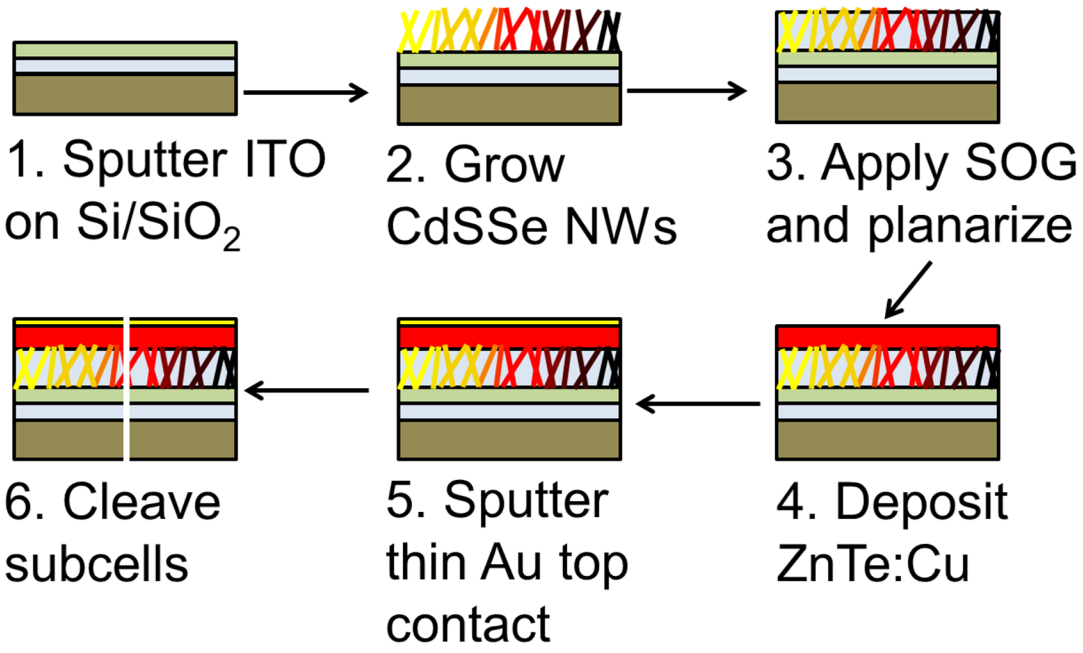

Figure III.D.2: Fabrication process for spatially composition-graded CdSSe thin film and nanowire solar cells with two subcells [32].

Spatially composition graded CdSSe nanowires were grown on Si/SiO_2/ITO substrates by Dual-Gradient CVD using Au catalyst. The growth setup is shown schematically in Fig. I.D.1. Electronic grade (99.99% pure) CdS and CdSe powders were used as the precursors and were placed in miniature quartz tubes within the larger furnace tube to create a spatial composition gradient in the source vapor impinging on the substrate. The nominal source temperatures were 700˚C and 630˚C for CdS and CdSe, respectively. The substrate was placed approximately 5 mm from the ends of the minitubes at a temperature of approximately 540˚C. Ar/H_2 (5% H_2 by molar ratio) carrier gas was flowed through the tube at a constant rate of 100 sccm, and the system pressure was maintained at 5.0 ± 0.1 Torr. The target temperature was maintained for a growth time of one hour, after which the system was allowed to cool gradually.

The composition-graded CdSSe films were grown in a similar manner, however no Au catalyst was used. Additionally, the CdS and CdSe source temperatures were increased to 900˚C and 775˚C, respectively, with the substrate temperature in the range of 370-400˚C.

The final step in the fabrication process was to cleave the sample at the location where the band gap reached the desired value to create two separate subcells. The band gap was measured as a function of position by photoluminescence (PL) scan, as described in section III.D.ii. In order to provide similar levels of above-band gap photon flux to both subcells during the filtered I-V measurements, the location for subcell cleaving was chosen to correspond to a wavelength of approximately 620 nm.

III.D.ii. Materials Characterization

The spatially composition-graded CdSSe nanowires and films were characterized by microphotoluminescence (micro-PL) scan using a 405 nm continuous-wave laser with a spot size less than 50 μm. Fig. III.D.3 shows the normalized PL spectra for a CdSSe nanowire ensemble (a) and film (b). As for all CdSSe film samples that were grown, the PL emission spectra in Fig. III.D.3(b) were dominated by defect emission in the 720-800 nm regime. The ratio of band edge to mid-gap emission for this sample was approximately 1 to 7. In contrast, many of the CdSSe nanowire ensembles showed spectra dominated by band edge emission. One such example is shown in Fig. III.D.3(a), where it was roughly three times stronger than the defect emission. Thus, the band edge emission for the nanowire ensemble in Fig. III.D.3 was roughly 20 times stronger than for the film, indicating that the optical quality of the nanowire materials was superior. The quality of the active materials is crucial because it plays a large role in determining

the ultimate efficiency of the device, and the superior quality of the nanowires in this case suggests they should provide an advantage over films for achieving high efficiencies in future MILAMB cells.

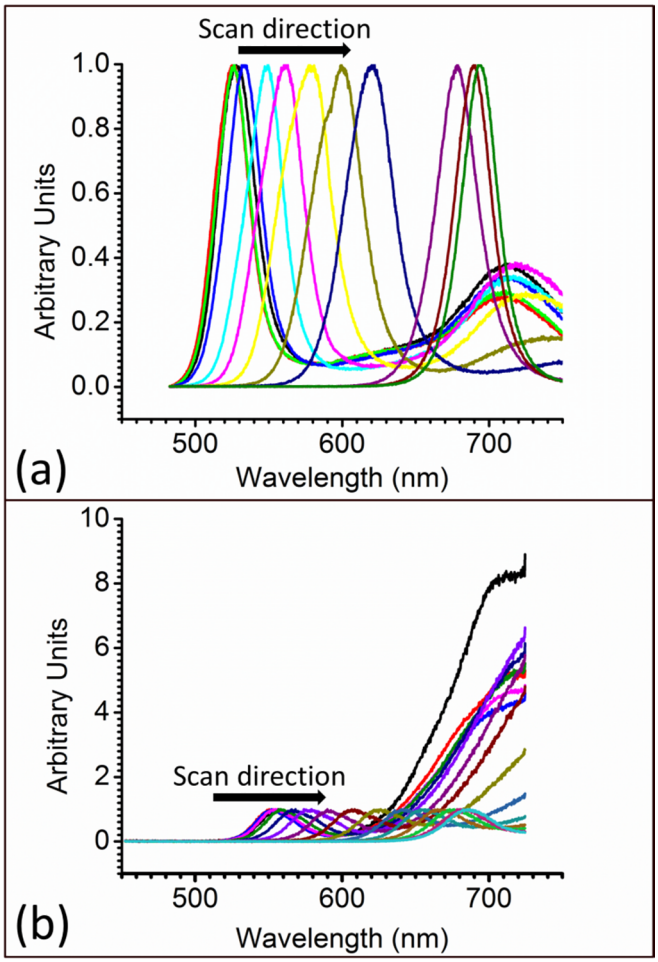

Figure III.D.3: Normalized micro-PL scans of a CdSSe (a) nanowire ensemble (sample 05222013N) and (b) film (sample 08272013X) grown on Si/SiO_2/ITO substrates, from [32].

Fig. III.D.4 shows the band gaps extracted from PL as a function of position. The CdSSe nanowires demonstrated continuous band gap variation from 1.79 to 2.36 eV, spanning virtually the entire range available with this materials system. The films tended to be somewhat more Se-rich, with band gaps in the range of 1.79 to 2.21 eV. Band gap

versus position data extracted from PL was used to determine where to cleave the samples to achieve subcell isolation.

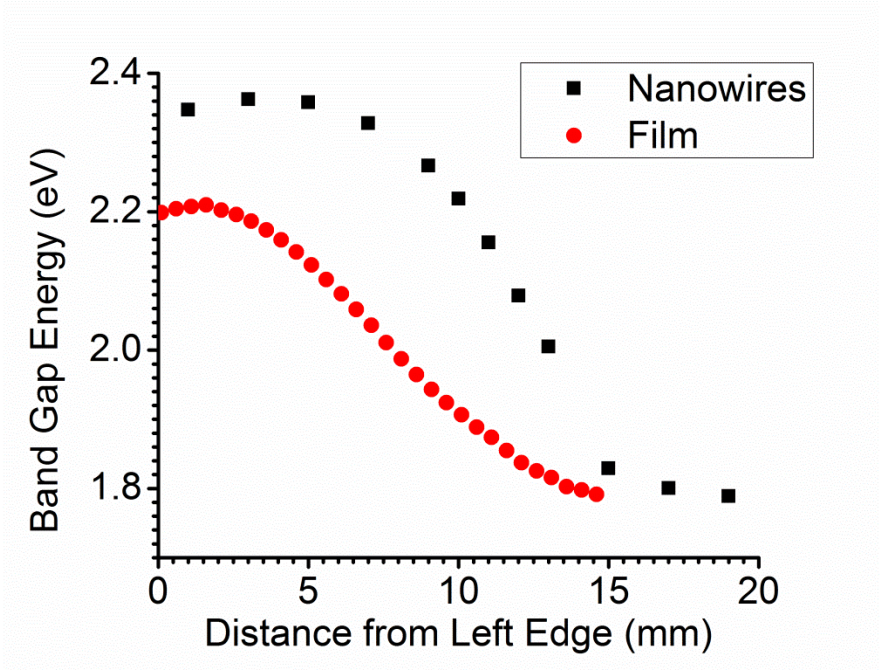

Figure III.D.4: Band gap extracted from micro-PL scan versus position for spatially composition-graded CdSSe nanowire and film samples from [32].

III.D.iii. I-V Results

The cells were mounted on glass stages and bonded to Au electrodes using Ag epoxy. I-V measurements were then performed under 1 sun AM1.5G illumination using a 4 mm diameter aperture placed over the smallest band gap region of the cells. Their performance is summarized in Table III.D.1, and the I-V characteristics of representative nanowire and thin film cells are shown in Fig. III.D.5 and III.D.6, respectively.

Table III.D.1: I-V performance data for spatially composition-graded CdSSe nanowire ensemble and thin film solar cells under 1 sun AM1.5G illumination. Results obtained using optical filters to simulate basic spectrum-splitting are shown in parentheses.

Sample ID	Cell Type	V_{oc} (mV)	J_{sc} (mA/cm^2)	FF
0522N	CdS-rich NWs (thick SU-8)	307 (*279*)	1.03×10^{-3} (5.48×10^{-4})	30.7% (*31.1%*)
	CdSe-rich NWs (thick SU-8)	133 (*74*)	1.43×10^{-4} (2.74×10^{-5})	34.3% (*30.1%*)
0219B	CdS-rich NWs	175 (*151*)	0.037 (*0.019*)	42.9% (*41.1%*)
	CdSe-rich NWs	173 (*132*)	0.162 (*0.050*)	41.2% (*37.7%*)
0219C	CdS-rich NWs	172 (*145*)	0.091 (*0.039*)	40.7% (*38.7%*)
	CdSe-rich NWs	136 (*70*)	0.349 (*0.109*)	32.3% (*26.7%*)
1122AG	CdS-rich NWs	142 (*119*)	0.046 (*0.024*)	37.7% (*35.9%*)
	CdSe-rich NWs	83 (*24*)	0.089 (*0.015*)	29.7% (*25.7%*)
0219D	CdS-rich NWs	85 (*56*)	0.045 (*0.020*)	30.6% (*27.9%*)
	CdSe-rich NWs	92 (*46*)	0.974 (*0.337*)	29.7% (*26.4%*)
0827O	CdS-rich film	78 (*55*)	0.530 (*0.268*)	33.2% (*31.0%*)
	CdSe-rich film	54 (*15*)	1.152 (*0.226*)	29.3% (*25.8%*)
0827X	CdS-rich film	14 (*8*)	0.286 (*0.144*)	25.2% (*24.9%*)
	CdSe-rich film	23 (*6*)	0.354 (*0.081*)	25.1% (*24.5%*)

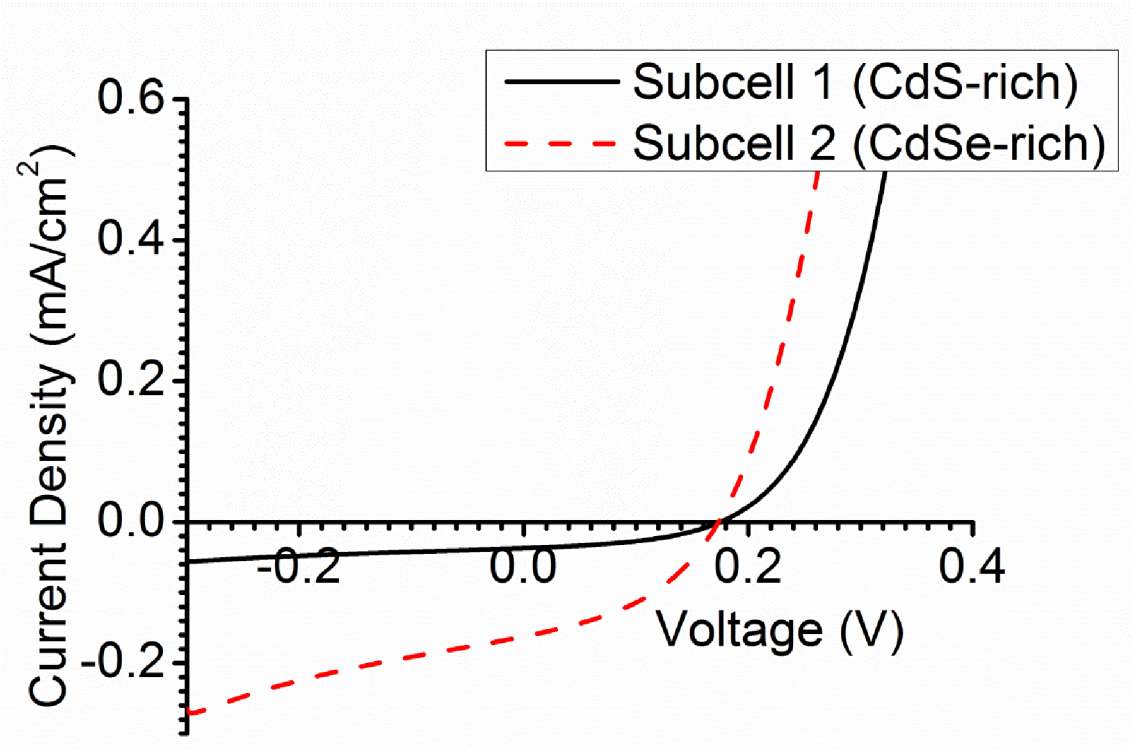

Figure III.D.5: I-V characteristics of composition-graded CdSSe nanowire cells (sample 0219B) for both the CdS- and CdSe-rich subcells under 1 sun AM1.5G illumination [32].

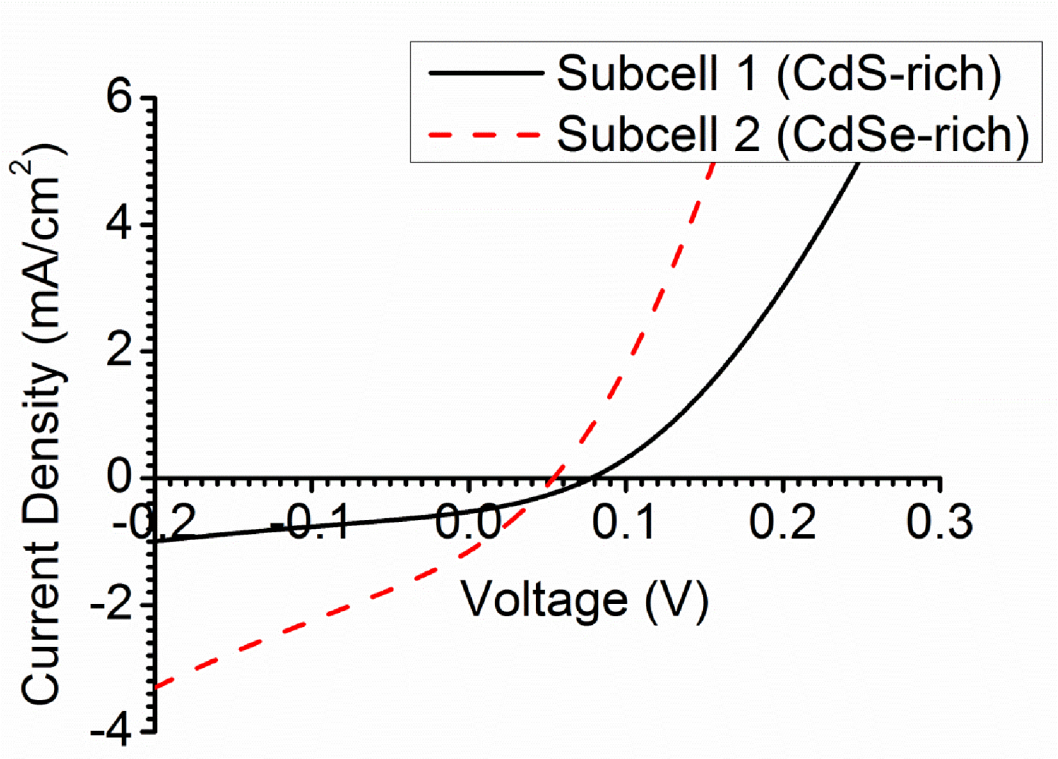

Figure III.D.6: I-V characteristics of composition-graded CdSSe film cells (sample 0827O) for both the CdS- and CdSe-rich subcells under 1 sun AM1.5G illumination [32].

Both the V_{oc} and FF of the CdSSe nanowire cells were superior to the CdSSe thin film cells. V_{oc}'s achieved by the CdS- and CdSe-rich nanowire cells were as high as 307 and 173 mV, respectively, and were on average approximately three times those of the film cells for both subcells. The nanowire cells also demonstrated FF over 40% for both subcells, whereas FF remained below 35% for the film cells. This is attributed to the superior optical quality of the nanowires, as shown in Fig. III.D.3, and suggests that in the long term, nanowires are preferable to films for implementing the MILAMB solar cell concept and could achieve higher efficiencies.

The J_{sc} of the nanowire cells was promising for unaligned nanowire ensembles and approached those of the film cells in the case of some CdSe-rich subcells. However, typical values for the nanowire cells tended to be somewhat lower than the corresponding

film cells. This was especially true in the case of the CdS-rich subcells, where the average J_{sc} of the nanowire cells was lower by roughly a factor of nine, as compared to a mere factor of two for the CdSe-rich subcells. The discrepancy in J_{sc} between film and nanowire cells is attributed to spin-on glass covering some of the wires, as discussed for the pure CdSe cells. Further confirmation of this is found in Table III.D.1. Sample 0522N was fabricated using relatively thick SU-8 as the spin-on dielectric, which was observed by SEM in Fig. III.C.3 to bury most of the nanowires. The J_{sc}'s for this sample were several orders of magnitude lower than the other nanowire cells in Table III.D.1, all of which were fabricated using thinner MSQ (see Fig. III.C.4), however the V_{oc} was relatively high. As discussed for the pure CdSe cells in Section III.C.iv, the simultaneous observation of much lower J_{sc} and similar or higher V_{oc} for SU-8 cells is indicative of SU-8 burying many nanowires. This is because V_{oc} depends logarithmically on J_{sc}. For a given cell, a lower J_{sc} should produce a lower V_{oc}. However, the relevant J_{sc} for determining V_{oc} is the microscopic J_{sc} within individual nanowires, not the measured J_{sc}, which is averaged over the entire illuminated area containing both contacted and uncontacted wires. The observation that cells fabricated with SU-8 have similar or higher V_{oc} to the other cells fabricated with MSQ suggests that the microscopic J_{sc} in individual wires is similar in both cases. This implies that the huge discrepancy in measured J_{sc} is due to differences in the number of nanowires contacted by the ZnTe layer, as supported by SEM in Fig. III.C.3. Given the clear evidence that SU-8 reduced the J_{sc} of cells by burying many of the nanowires, it is logical to extend this argument to the cells fabricated with MSQ, which although considerably thinner than SU-8 was still relatively thick at 4

μm. This explains why the nanowire cells fabricated with MSQ have lower J_{sc} than the film cells but much higher J_{sc} than nanowire cells fabricated with SU-8.

This can also explain the discrepancy in J_{sc} between the CdS- and CdSe-rich nanowire cells. As shown in Fig. III.D.7 below, the morphology of the CdS-rich compositions tended to favor smaller, thinner nanowires organized in dense networks. The CdSe-rich compositions, in contrast, favored larger, tapered nanobelts. The larger structures in the CdSe-rich region were more likely to penetrate the full thickness of the MSQ layer, and therefore a greater number of them contacted the ZnTe layer to form an active part of the device. Thus, the CdSe-rich nanowire cells tended to have higher J_{sc} than their CdS-rich counterparts.

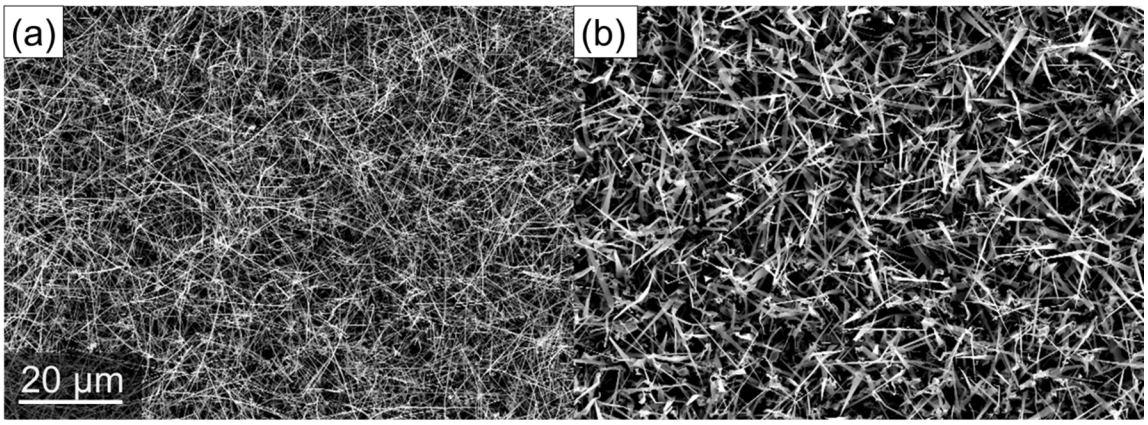

Figure III.D.7: SEM images (1000x magnification) of spatially composition-graded CdSSe nanowires in the (a) CdS-rich and (b) CdSe-rich regions.

I-V measurements were also taken under filtered illumination using BG-18 and R-62 optical filters to simulate a simple form of spectrum-splitting and provide similar levels of above-band gap photon flux to both cells (maximum potential photocurrent of roughly 6 mA/cm^2, neglecting the opacity of the top contact). The results are given in Table

III.D.1 in parentheses. I-V characteristics for both subcells of a CdSSe nanowire solar cell (sample 0219B) are shown in Fig. III.D.8.

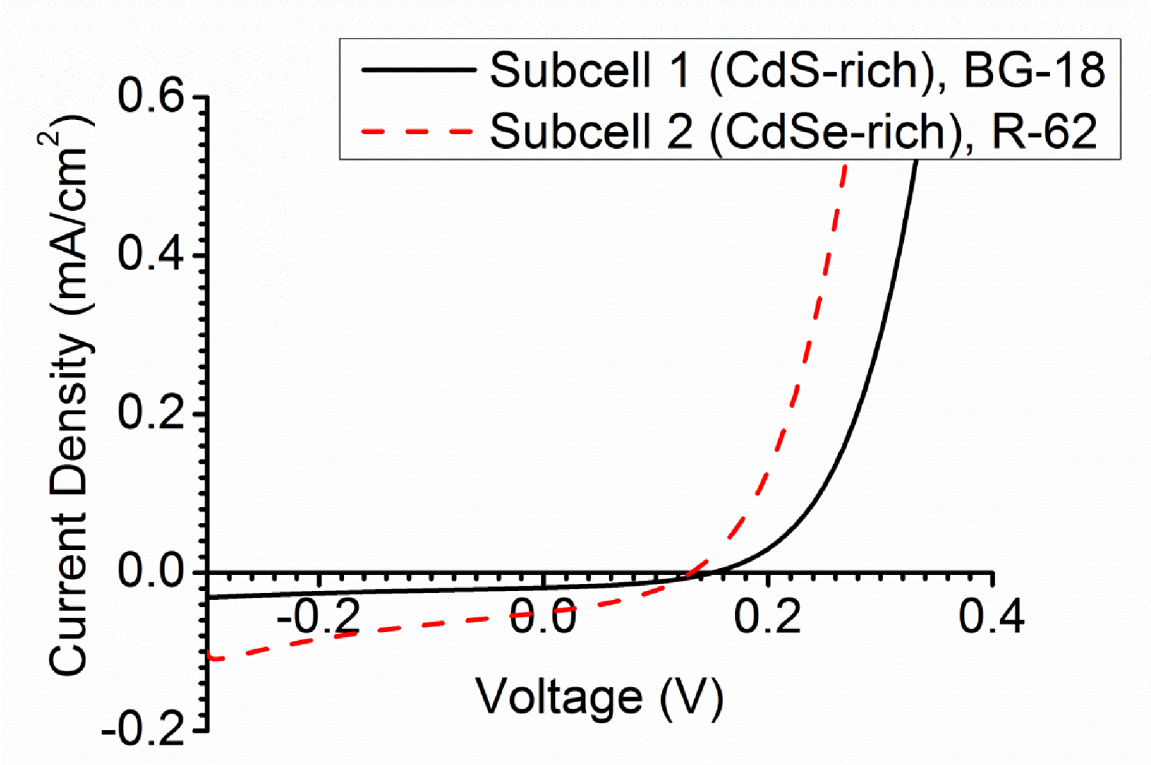

Figure III.D.8: I-V characteristics of composition-graded CdSSe nanowire cells (sample 0219B) for both the CdS- and CdSe-rich subcells under 1 sun AM1.5G illumination with optical filters to simulate a simple form of spectrum-splitting [32].

An examination of Table III.D.1 shows that under filtered illumination, the CdS-rich cells had uniformly higher V_{oc} and FF than their CdSe-rich partners, unlike the case for unfiltered illumination. This was expected, since the CdS-rich subcell has a wider band gap and should therefore have a higher V_{oc} and FF for a given J_{sc}. The optical filters ensured both cells received similar above-band gap photon flux, so it is believed that the J_{sc} within individual nanowires was similar for both, assuming their quantum efficiencies were similar. This suggests that if all nanowires can be contacted and the location of subcell isolation fine-tuned to achieve current-matching, the wide-gap CdS-rich cell

would produce greater output power density than the narrower-gap CdSe-rich cell, which is the chief benefit of spectrum-splitting that enables high efficiencies to be achieved. This constitutes a proof-of-concept demonstration of a MILAMB solar cell with two subcells fabricated simultaneously on a single substrate using spatially composition-graded alloy nanowires.

III.E. Comparison of Pure CdSe and CdSSe Cells

A comparison among the various types of cells reported in this dissertation shows that the pure CdSe film cells achieved the best performance, followed by the CdSSe and pure CdSe nanowire cells, and lastly the CdSSe film cells. For the nanowire ensemble cells, pure CdSe cells showed performance roughly comparable to the CdSe-rich CdSSe subcells. However, for film cells, the pure CdSe cells achieved much better I-V performance than the CdSe-rich CdSSe cells.

The superior performance of the pure CdSe film cells as opposed to the nanowire cells in this dissertation was attributed to faster surface recombination in the nanowire cells. As previously discussed, time-correlated single photon counting measurements of pure CdSe films and nanowires revealed that the films had carrier lifetimes of approximately 0.8 ns, as compared to just 0.4 ns for the nanowires. Since the compositions of both were the same, this difference was attributed to morphology, which implicated higher levels of surface recombination in the nanowires as the culprit. The large surface areas of the nanowires increased the rate of surface recombination and decreased the overall carrier lifetime, giving the pure CdSe films an advantage that resulted in better I-V performance.

Meanwhile, the discrepancy in performance between the nanowire cells and the CdSSe film cells was attributed to poor material quality in the composition-graded films. The much higher optical quality of the composition-graded CdSSe nanowires as compared to the CdSSe films, as revealed by a comparison of their photoluminescence spectra in Fig. III.D.3, suggests that the bulk crystal quality in the composition-graded CdSSe films was much worse. This suggests that composition-grading may be detrimental to the material quality in films, in contrast to nanowires, where the composition-graded materials were of relatively high quality. This underscores the long term importance of using nanowires rather than films to implement the MILAMB solar cell concept.

III.F. Conclusion

Two solar cells with different band gaps were fabricated simultaneously on a single substrate using spatially composition-graded CdSSe alloy nanowires grown in a single step by the Dual Gradient Method. CdS- and CdSe-rich subcells demonstrated V_{oc} up to 307 and 173 mV and J_{sc} up to 0.091 and 0.974 mA/cm^2 under 1 sun AM1.5G illumination, respectively. I-V measurements performed under filtered illumination to simulate a simple form of spectrum-splitting showed that the wide-gap CdS-rich cells had uniformly higher Voc and FF than their CdSe-rich partners. This suggested that the CdS-rich cells produced more power on the single-nanowire level than the CdSe-rich cells, as expected for the wider band gap subcell, which is the principal benefit of spectrum-splitting that enables high efficiencies to be obtained. These results constitute a proof-of-concept demonstration of MILAMB solar cells with two subcells fabricated

simultaneously in the same process flow on one substrate using composition-graded nanowire materials grown by the Dual Gradient Method.

Considerable work remains before the MILAMB solar cell concept could result in a practical system, but it is hoped that the work in this dissertation has laid some of the foundations for future research. Fabricating multiple solar cells simultaneously on one substrate using single crystal nanowire materials spanning a wide range of band gap energies and grown in a single, inexpensive step by the Dual Gradient Method could help to reduce the cost and complexity of manufacturing cells for spectrum-splitting photovoltaic systems. Moreover, the potential to increase the number of subcells without significantly increasing the cost or complexity of fabrication could help to partially decouple the cost of the system from its efficiency. In this way, the MILAMB approach to fabricating multiple solar cells for spectrum-splitting photovoltaic systems could provide an inexpensive alternative to multi-junction tandem cells for achieving high power conversion efficiencies.

CHAPTER IV

RECOMMENDATIONS FOR FUTURE RESEARCH

In this dissertation, proof-of-concept devices with two subcells fabricated simultaneously on a single substrate were demonstrated. However, further research is required before this could result in a practical system. The remaining challenges include growing composition-graded materials spanning the full range of band gaps required for spectrum-splitting photovoltaics; designing and fabricating an appropriate structure for separating photogenerated charge carriers across a broad range of compositions in those materials; obtaining high interface quality at the p-n junction and low surface recombination for improving charge collection and device performance; contacting all nanowires in the ensemble; finding low cost and high throughput and yield solutions to various processing steps, including contact isolation (presently achieved with a spin-on dielectric); and designing and fabricating low cost dispersive optics with high efficiency (> 90%) across a broad wavelength range (~500-1800 nm) to match the composition-grading in the semiconductor layer.

In the near term, the primary focus should be on additional materials research to develop nanowire absorption materials suitable for cells spanning the entire solar spectrum. The nanowires should be of high crystal quality, with long diffusion lengths to facilitate charge separation. Potential p-n homo- or heterojunction structures should be evaluated at an early stage, and different compositions should be suited to the same dopants or heterojunction partner materials whenever possible. For nanowire materials capable of both p- and n-type doping, homojunction structures would have a significant advantage, since heterojunction partner materials suitable for such a broad range of alloy

compositions and band gaps may not be available, and heterojunctions tend to introduce interface states at the junction. Both CdPbS and InGaN were discussed as potential options in this dissertation. In the case of CdPbS, alloying across the full composition range has not yet been accomplished, and it is unclear whether this goal can be achieved. Efforts so far using the Dual-Gradient Method have demonstrated $Cd_xPb_{1-x}S$ with x no greater than 0.14 [33]. In the case of InGaN, nanowires spanning the entire composition range from InN to GaN have already been demonstrated, although the absorption edge for In-rich compositions remained above 1.0 eV [31]. For both systems, the junction structures could be challenging. The preliminary designs in this dissertation are based on energy band alignments derived from Anderson's model using the electron affinities, but this model is not reliable without experimental verification. Additional work is also required to demonstrate sufficient carrier lifetimes to fabricate a high efficiency device, and typical defect densities and surface recombination rates should be considered in the selection of materials.

Another critical issue is the device structure and interface quality. Obtaining low interface recombination rates at the junction is critical for achieving high efficiencies. If the p-n junction comprises a heterojunction structure, this would likely require the heterojunction partner material to be grown epitaxially on the nanowire materials. This could be done in either a core-shell or axial junction configuration. Both have advantages and disadvantages, depending on the properties of the specific system. For nanowires with high surface recombination, surface depletion, or other effects which can decrease charge separation efficiency, the core-shell structure can be advantageous by reducing the collection length without reducing the optical thickness available for light absorption

[67]. The trade-off is that this entails a many-fold increase in the junction area without increasing the light collection area, which increases the dark current. For nanowire cells where the collection efficiency is a concern, the increase in J_{sc} and V_{oc} due to better charge separation using the core-shell structure can be a net benefit. In cells where this is less of a problem, an axial junction may be preferable, and record-performing InP-based nanowire solar cells demonstrated recently have used this approach [68]. In principle, axial junction nanowire array solar cells could actually achieve higher efficiencies than similar film cells because the junction area can be much lower for the same light collection area, while still achieving full optical absorption. The choice between these two device structures will depend upon the specific properties of the selected materials, but they share the requirement for high interface quality.

Electrically contacting the nanowires while avoiding shunting between the electrodes is another critical issue and has already been discussed for the devices fabricated in this work. A reliable and inexpensive scheme must be devised to allow all the nanowires to be contacted, and the bottom electrode must be isolated in some way from the top electrode. In this work and some others in literature [69]-[72], this was accomplished by applying a spin-on dielectric material to fill the voids between wires, planarizing, and depositing additional device layers on top. This requires growing vertically aligned wires in order to ensure that all are contacted. Due to the wide range of compositions and lattice constants required on a single substrate, growth templates may be the best option for accomplishing this (since epitaxial growth from the substrate is not an option). In any case, depending on the level of solar concentration in the final application, the spin-on dielectric method may not be economical in production due to the high cost of many of these materials.

Lower cost materials or alternative methods may therefore be required, and the best option may depend on the nanowire materials.

Lastly, additional research is necessary to develop inexpensive and high efficiency optics, preferably with flat panel form factor, to match the dispersion pattern of the light to the composition grading of the nanowires. There are a number of technologies that could be employed, including refractive and holographic elements, but it will be critical to ensure high optical efficiency over a very broad wavelength range. This is partly a co-optimization problem, so the design of the optics and cells will need to be integrated.

REFERENCES

[1] R.L. Moon et al., "Multigap solar cell requirements and the performance of AlGaAs and Si cells in concentrated sunlight," 13th IEEE Photovoltaic Specialists Conference, Washington, D.C., 5-8 June 1978.

[2] X. Wang et al., "Improved Outdoor Measurements for Very High Efficiency Solar Cell Sub-Modules," 34th IEEE Photovoltaic Specialists Conference, Philadelphia, PA, 7-12 June 2009.

[3] B. Mitchell et al., "Four-junction spectral beam-splitting photovoltaic receiver with high optical efficiency," *Progress in Photovoltaics: Research and Applications* **19**, 61-72 (2011).

[4] X. Wang et al., "Lateral spectrum splitting concentrator photovoltaics: direct measurement of component and submodule efficiency," *Progress in Photovoltaics: Research and Applications* **20**, 149-165 (2012).

[5] M.A. Green and A.Ho-Baillie, "Forty three per cent composite split-spectrum concentrator solar cell efficiency," *Progress in Photovoltaics: Research and Applications* **18**, 42-47 (2010).

[6] A. Barnett et al., "50% Efficient Solar Cell Architectures and Designs," 4th IEEE World Conference on Photovoltaic Energy Conversion, Waikoloa, HI, 7-12 May 2006.

[7] A. Barnett et al., "Milestones Towards 50% Efficient Solar Cell Modules," presented at the 22nd European Photovoltaic Specialists Conference, Milan, Italy, 3 September 2007.

[8] H.A. Atwater et al., "Full Spectrum Ultrahigh Efficiency Photovoltaics," 39th IEEE Photovoltaic Specialists Conference, Tampa, FL, June 16-21 2013.

[9] C.Z. Ning, A.L. Pan, and R.B. Liu, "Spatially composition-graded alloy semiconductor nanowires and wavelength specific lateral-multijunction full-spectrum solar cells," 34th IEEE Photovoltaic Specialists Conference, Philadelphia, PA, 7-12 June 2009.

[10] A.L. Pan, W. Zhou, E.S.P. Leong, R.B. Liu, A.H. Chin, B. Zou, and C.Z. Ning, "Continuous Alloy-Composition Spatial Grading and Superbroad Wavelength-Tunable Nanowire Lasers on a Single Chip", *Nano Letters* **9**, 784-788 (2009).

[11] A.L. Pan, R.B. Liu, M. Sun, and C.Z. Ning, "Spatial Composition Grading of Quaternary ZnCdSSe Alloy Nanowires with Tunable Light Emission between 350 and 710 nm on a Single Substrate", *ACS Nano* **4**, 671-680 (2010).

[12] D. Caselli and C.Z. Ning, "High-performance laterally-arranged multiple-bandgap solar cells using spatially composition-graded $Cd_xPb_{1-x}S$ nanowires on a single substrate: a design study," *Optics Express* **19** (S4), A686-A694 (2011).

[13] D. Caselli and C.Z. Ning, "Full-Spectrum Laterally Arranged Multiple-Bandgap InGaN Solar Cells," 38th IEEE Photovoltaic Specialists Conference, Austin, TX, 3-8 June 2012.

[14] R.F. Pierret, *Semiconductor Device Fundamentals* (Addison-Wesley Publishing Company, Reading, MA, 1996).

[15] C.T. Sah, R.N. Noyce, and W. Shockley, "Carrier Generation and Recombination in P-N Junctions and P-N Junction Characteristics," *Proceedings of the IRE* **45** (9), 1228-1243 (1957).

[16] ATLAS, version 5.15.34.C, Silvaco Data Systems, Inc.: 2009.

[17] C. Honsberg and S. Bowden, PVCDROM, 2010, Accessed 29 June 2011, http://pveducation.org/pvcdrom

[18] W.H. Shockley and H.J. Queisser, "Detailed Balance Limit of Efficiency of p-n Junction Solar Cells," *Journal of Applied Physics* **32** (3), 510-519 (1961).

[19] C.H. Henry, "Limiting efficiencies of ideal single and multiple energy gap terrestrial solar cells," *Journal of Applied Physics* **51** (8), 4494-4500 (1980).

[20] J.J. Loferski, "Theoretical Considerations Governing the Choice of Optimum Semiconductor for Photovoltaic Solar Energy Conversion," *Journal of Applied Physics* **27** (7), 777-784 (1956).

[21] A. De Vos, "Detailed balance limit of the efficiency of tandem solar cells," *Journal of Physics D: Applied Physics* **13**, 839-846 (1980).

[22] A.G. Imenes and D.R. Mills, "Spectral beam splitting technology for increased conversion efficiency in solar concentrating systems: a review," *Solar Energy Materials & Solar Cells* **84**, 19-69 (2004).

[23] B. Mitchell et al., "Four-junction spectral beam-splitting photovoltaic receiver with high optical efficiency," *Progress in Photovoltaics: Research and Applications* **19**, 61-72 (2011).

[24] W.H. Bloss, M. Griesinger, and E.R. Reinhardt, "Dispersive concentrating systems based on transmission phase holograms for solar applications," *Applied Optics* **21** (20), 3739-3742 (1982).

[25] J.E. Ludman et al., "The Optimization of a Holographic System for Solar Power Generation," *Solar Energy* **60** (1), 1-9 (1997).

[26] R.K. Kostuk and G. Rosenberg, "Analysis and Design of Holographic Solar Concentrators," Proceedings of SPIE 7043, 70430I (2008).

[27] R.K. Kostuk et al., "Spectral shifting and holographic planar concentrators for use with photovoltaic solar cells," Proceedings of SPIE 6649, 66490I (2007).

[28] J.M. Castro, D. Zhang, and R.K. Kostuk, "Planar Holographic Solar Concentrators for Low and Medium Ratio Concentration System," in Optics for Solar Energy, OSA Technical Digest (CD) (Optical Society of America, 2010), paper STuB3.

[29] T. Gu and M.W. Haney, "Ultra-compact Dispersive Concentrator Concept for Laterally-arrayed Multi-junction PV Cells," Renewable Energy and the Environment, Tucson, AZ, 11-14 November 2012.

[30] A. L. Pan, R.B. Liu, M.H. Sun, and C.Z. Ning, "Quaternary Alloy Semiconductor Nanobelts with Band gap Spanning the Entire Visible Spectrum," *Journal of the American Chemical Society* (Communication) **131**, 9502 (2009), DOI: 10.1021/ja904137m

[31] T. Kuykendall et al., "Complete composition tunability of InGaN nanowires using a combinatorial approach," *Nature Materials* **6**, 951-956 (2007).

[32] D. Caselli, Z. Liu., D. Shelhammer, and C.Z. Ning, "Composition-Graded Nanowire Solar Cells Fabricated in a Single Process for Spectrum-Splitting Photovoltaic Systems," *Nano Letters*, preprint, 9 Sept. 2014, doi: 10.1021/nl502662h.

[33] P.L. Nichols, "Growth and Characterization of Chalcogenide Alloy Nanowires with Controlled Spatial Composition Variation for Optoelectronic Applications" (2012), ASU Electronic Dissertations and Theses. http://hdl.handle.net/2286/R.I.15881

[34] H. Rahnamai and J.N. Zemel, "PbS – Si heterojunction II: electrical properties," *Thin Solid Films* **74** (1), 17-22 (1980).

[35] Z. Liu et al., "Room temperature photocurrent response of PbS/InP heterojunction," *Applied Physics Letters* **95** (23), 231113 (2009).

[36] ATLAS User's Manual: Device Simulation Software (SILVACO International, 2007).

[37] T.L. Chu and S.S. Chu, "Thin film II VI photovoltaics," *Solid State Electronics* **38** (3), 533-549 (1995).

[38] U.V. Desnica, "Doping Limits in II-VI Compounds – Challenges, Problems and Solutions," *Progress in Crystal Growth and Characterization of Materials* **36** (4), 291-357 (1998).

[39] H. Ohta et al., "Highly electrically conductive indium-tin-oxide thin films epitaxially grown on yttria-stabilized zirconia (100) by pulsed-laser deposition," *Applied Physics Letters* **76** (19), 2740-2742.

[40] Y. Imai, A. Watanabe, and I. Shimono, "Comparison of electronic structures of ZnS and ZnO calculated by a first-principle pseudopotential method," *Journal of Materials Science: Materials Science in Electronics* **14** (3), 149-156 (2003).

[41] R. Swank, "Surface Properties of II-VI Compounds," *Physical Review* **153** (3), 844-849 (1967).

[42] W.M Haynes, ed., *CRC Handbook of Chemistry and Physics*, 93rd Edition (Internet Version 2013), CRC Press/Taylor and Francis, Boca Raton, FL.

[43] Siklitsky, Vadim (2001), "Electronic Archive: New Semiconductor Materials, Characteristics, and Properties," Ioffe Physico-Technical Institute [Online], Available: http://www.ioffe.ru/SVA/NSM/.

[44] K. Emery and D. Meyers, "Solar Spectral Irradiance: Air Mass 1.5," National Renewable Energy Laboratory, 2009, Accessed 2009, http://rredc.nrel.gov/solar/spectra/am1.5/ASTMG173/ASTMG173.html.

[45] M.D. Kelzenberg et al., "Enhanced absorption and carrier collection in Si wire arrays for photovoltaic applications," *Nature Materials* **9**, 239-244 (2010).

[46] N. Lagos, M.M. Sigalas, and D. Niarchos, "The optical absorption of nanowire arrays," *Photonics and Nanostructures – Fundamentals and Applications* **9**, 163-167 (2011).

[47] A. Niemegeers and M. Burgelman, "Effects of the Au/CdTe back contact on IV and CV characteristics of Au/CdTe/CdS/TCO solar cells," *Journal of Applied Physics* **81** (6), 2881-2886 (1997).

[48] G.F. Brown et al., "Finite element simulations of compositionally graded InGaN solar cells," *Solar Energy Materials and Solar Cells* **94**, 478-483 (2010).

[49] J. Mickeviius et al., "Time-resolved experimental study of carrier lifetime in GaN epilayers," *Applied Physics Letters* **87**, 241918 (2005).

[50] P. Parkinson et al., "Noncontact Measurement of Charge Carrier Lifetime and Mobility in GaN Nanowires," *Nano Letters* **12**, 4600-4604 (2012).

[51] P.G. Moses and C.G. Van de Walle, "Band bowing and band alignment in InGaN alloys," *Applied Physics Letters* **96**, 021908 (2010).

[52] C.L. Wu, H.M. Lee, C.T. Kuo, C.H. Chen, and S. Gwo, "Cross-sectional scanning photoelectron microscopy and spectroscopy of wurtzite InN/GaN heterojunction: Measurement of "intrinsic" band lineup," *Applied Physics Letters* **92**, 162106 (2008).

[53] V.M. Bermudez, "Simple interpretation of metal/wurtzite-GaN barrier heights," *Journal of Applied Physics* **86** (2), 1170-1171 (1999).

[54] H.C. Casey, Jr., F. Ermanis, and K.B. Wolfstirn, "Variation of Electrical Properties with Zn Concentration in GaP," *Journal of Applied Physics* **40** (7), 2945-2958 (1969).

[55] F. Buch, A.L. Fahrenbruch, and R.H. Bube, "Photovoltaic properties of n-CdSe/p-ZnTe heterojunctions," *Applied Physics Letters* **28** (10), 593-595 (1976).

[56] N.G. Patel et al., "Fabrication and Characterization of ZnTe/CdSe Thin Film Solar Cells," *Crystal Research and Technology* **29** (2), 247-252 (1994).

[57] A.K. Pal, A. Mondal, S. Chaudhur, "Preparation and characterization of ZnTe/CdSe solar cells," *Vacuum* **41**, 1460-1462 (1990).

[58] K. Wang et al., "Nearly lattice matched all wurtzite CdSe/ZnTe type II core-shell nanowires with epitaxial interfaces for photovoltaics," *Nanoscale* **6**, 3679-3685 (2014).

[59] J.L. Pautrat et al., "Donors and Acceptors in Tellurium Compounds; The Problem of Doping and Self-Compensation," *Journal of Crystal Growth* **73**, 194-204 (1985).

[60] J. Tang, D. Mao, and J.U. Trefny, "Effect of Cu Doping on the Properties of ZnTe:Cu Thin Films and CdS/CdTe/ZnTe Solar Cells," CP394 NREL/SNL Photovoltaics Program Review, 639-646 (1997).

[61] T.A. Gessert et al., "Development of Cu-doped ZnTe as a back-contact interface layer for thin-film CdS/CdTe solar cells," *Journal of Vacuum Science and Technology A* **14** (3), 806-812 (1996).

[62] J. Zhang et al., "The structural phase transition and mechanism of abnormal temperature dependence of conductivity in ZnTe:Cu polycrystalline thin films," *Thin Solid Films* **414**, 113-118 (2002).

[63] J.Y.W. Seto, "The electrical properties of polycrystalline silicon films," *Journal of Applied Physics* **46** (12), 5247-5254 (1975).

[64] Fan, Z.; Ravazi, H.; Do, J.; Moriwaki, A.; Ergen, O.; Chueh, Y.L.; Leu, P.W.; Ho, J.C.; Takahashi, T.; Reichertz, L.A.; Neale, S.; Yu, K.; Wu, M.; Ager, J.W.; Javey, A. Three-dimensional nanopillar-array photovoltaics on low-cost and flexible substrates. *Nature Materials* **8**, 648-653 (2009).

[65] S. Hegedus, D. Desai, and C. Thompson, "Voltage Dependent Photocurrent Collection in CdTe/CdS Solar Cells," *Progress in Photovoltaics: Research and Applications* **15**, 587-602 (2007).

[66] K. Wang et al., "Conduction band offset at the InN/GaN heterojunction," *Applied Physics Letters* **91**, 232117 (2007).

[67] B.M. Kayes, H.A. Atwater, and N.S. Lewis, "Comparison of the device physics principles of planar and radial p-n junction nanorod solar cells," *Journal of Applied Physics* **97**, 114302 (2005).

[68] J. Wallentin et al., "InP Nanowire Array Solar Cells Achieving 13.8% Efficiency by Exceeding the Ray Optics Limit," *Science* **339**, 1057-1060 (2013).

[69] A.C.E. Chia and R.R. LaPierre, "Contact planarization of ensemble nanowires," *Nanotechnology* **22**, 245304 (2011).

[70] A.R. Abramson et al., "Fabrication and Characterization of a Nanowire/Polymer-Based Nanocomposite for a Prototype Thermoelectric Device," *Journal of Microelectromechanical Systems* **13** (3), 505-513 (2004).

[71] M.Y. Hsieh et al., "InGaN-GaN Nanorod Light Emitting Arrays Fabricated by Silica Nanomasks," *IEEE Journal of Quantum Electronics* **44** (5), 468-472 (2008).

[72] E. Latu-Romain et al., "A generic approach for vertical integration of nanowires," *Nanotechnology* **19**, 345304 (2008).